FRONTIERS OF PHYSICS

TOPICAL REVIEW
Volume 19 / Issue 6 / 63501 / 2024

Localized surface plasmon resonance enhanced photodetector: Physical model, enhanced mechanism and applications

Jiangtong Su[1,3], Xiaoqi Hou[2,3], Ning Dai[1,3,4,5,†], Yang Li[1,3,4,‡]

1 School of Physics and Optoelectronic Engineering, Hangzhou Institute for Advanced Study, University of Chinese Academy of Sciences, Hangzhou 310024, China
2 School of Chemistry and Materials Science, Hangzhou Institute for Advanced Study, University of Chinese Academy of Sciences, Hangzhou 310024, China
3 University of Chinese Academy of Sciences, Beijing 100049, China
4 Research Institute of Intelligent Sensing, Zhejiang Lab, Hangzhou 311100, China
5 Shanghai Institute of Technical Physics, Chinese Academy of Sciences, Shanghai 200083, China
Corresponding authors. E-mail: †ndai@mail.sitp.ac.cn, ‡ly@ucas.ac.cn
Received November 15, 2023; accepted April 16, 2024

ABSTRACT

Localized surface plasmon resonance (LSPR) is an intriguing phenomenon that can break diffraction limitations and exhibit excellent light-confinement abilities, making it an attractive strategy for enhancing the light absorption capabilities of photodetectors. However, the complex mechanism behind this enhancement is still plaguing researchers, especially for hot-electron injection process, which inhibits further optimization and development. A clear guideline for basic physical model, enhancement mechanism, material selection and architectural design for LSPR photodetector are still required. This review firstly describes the mainstream understanding of fundamental physical modes of LSPR and related enhancement mechanism for LSPR photodetectors. Then, the universal strategies for tuning the LSPR frequency are introduced. Besides, the state-of-the-art progress in the development of LSPR photodetectors is briefly summarized. Finally, we highlight the remaining challenges and issues needed to be resolved in the future research.

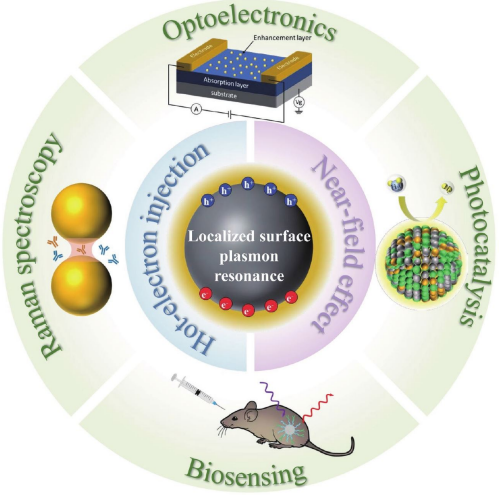

Keywords localized surface plasmon resonance, photodetector, plasmonic nanomaterials, hot electron

Contents

Higher Education Press

https://doi.org/10.1007/s11467-024-1413-8

1 Introduction

With Moore's law approaching its limit, silicon-based photoelectric integration has become an important direction for the development of semiconductor materials and technologies in the future. Semiconductor micro-nano photodetectors with small size, low power consumption and high sensitivity are regarded as the keys to the core detectors of the silicon-based photoelectric integration. Photodetector has promised an unprecedented class of optoelectronic devices due to its unique ability to absorb photons and convert them into electrical signals. Extensive efforts have been made to pursue various applications of photodetectors, including camera imaging [1], bio-sensing [2, 3], spectrometer [4], night vision [5, 6], and communication systems [7, 8]. Commercial photodetectors are generally manufactured by semiconductor bulk materials, such as Si for visible-light photodetectors and InGaAs/HgCdTe for infrared photodetectors. However, these materials are usually fabricated under high temperature and vacuum by molecular beam epitaxy or metal-organic chemical vapor deposition methods, which are costly and complicated. Also, with the increasing demand for next generation multi-functional photodetectors, these traditional semiconductor bulk materials are close to the limitation for further reducing the size, weight, and power consumption [9], improving their performance, and compatibility with flexible devices. Thus, it is urgent to break these bottlenecks with a new materials system. Due to the excellent light-harvesting, carrier transport, and flexibility, low-dimensional semiconductors, such as two-dimensional nanosheets (MoS_2, graphene, etc. [10–14]), one-dimensional nanowires/nanoribbons (Si, ZnO, GaN, etc. [15–21]) and zero-dimensional quantum dots (CdSe, PbS, HgTe, etc. [22–25]), have been greatly developed for achieving high photodetector performance in terms of high responsibility, fast response speed, and broad response range. However, the reduced size of devices leads to inefficient light absorption due to the physics limitations, resulting in relatively low photoelectric conversion efficiency. Therefore, it is important to develop an effective localized field control method for achieving high-performance low-dimensional photodetector.

Surface plasmon, i.e., a special light–matter interaction

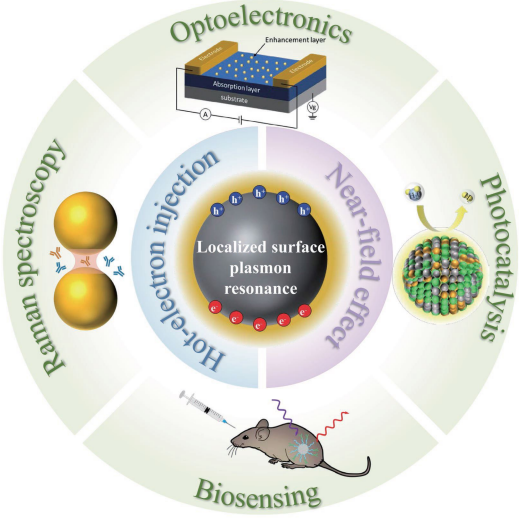

Fig. 1 Schematic, enhancement mechanism and applications of LSPR.

that can achieve efficient light concentration at subwavelength [26], offers a promising strategy to get over the dilemma of the low-dimensional photodetectors because of its unique capability of concentrating, routing, and manipulating light at the nanoscale [27]. Surface plasmon is a collective oscillation formed by the interaction of free electrons and photons on the interface region between metal/semiconductor and a dielectric medium (such as a metal layer in the air). Once excited by direct illumination, a non-propagating excitation of the conduction electrons is localized on the material's surface, known as localized surface plasmon resonance (LSPR). The LSPR can induce near-field effect and hot-electron injection. The near-field effect significantly enhances the surface electric field intensity of LSPR materials, allowing light to surpass the diffraction limit and achieving efficient light focusing. Hot electron injection process converts the energy of electromagnetic waves into plasmonic resonances of electrons, then the hot electrons are transferred to the absorption layer of photoelectric devices, which effectively enhances the utilization of light by photonic devices. These excellent characteristic has attracted great interest in a wide range of fields, including optoelectronics [28, 29], photocatalysis [30–32], spectroscopy [33–35], single-molecule sensing [36–38], surface-enhanced Raman scattering (SERS) [39, 40], and optical-switch [41]. Thus, lots of works have demonstrated the validity of enhancing the device performance of low-dimensional photodetectors via LSPR effects [42–44]. By well designing the size and geometry of plasmonic materials structures, the LSPR effects can cover a broad window ranging from the UV to infrared region. Furthermore, plasmonic materials can be fabricated by a simple process according to the dimensions of the photodetector. These excellent properties of LSPR effects make plasmonic

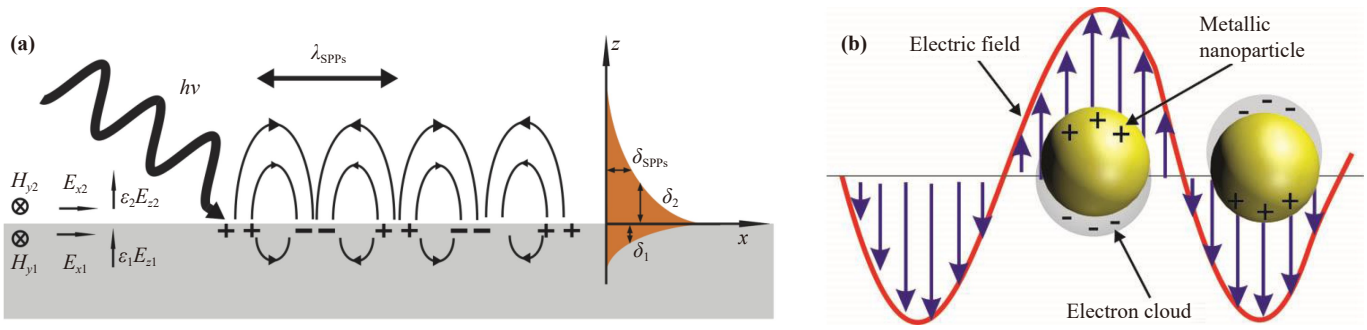

Fig. 2 **(a)** Schematic of the physical model of surface plasmon polaritons (SPPs) at the interface of two medias. The electromagnetic wave propagates along the x direction of the surface. These vectors (H_{y2}, E_{x2}) represent the direction of the electric and magnetic field. The orange area illustrates the field intensity distribution, which reveals that the field is focused around the surface and decays exponentially along the z direction. **(b)** Schematic of the physical model of LSPRs in nanoparticles. Reproduced from Ref. [48].

photodetectors promising candidates for new generation photoelectric detection.

In this review, we will give a systematic description of the physical model of LSPR, underlying the mechanisms of LSPR enhanced photodetectors, and summarize the recent progress on LSPR enhanced photodetectors. We will first introduce the basic physical models of surface plasmon, illustrating two kinds of excitation modes, i.e., surface plasmon polaritons (SPPs) and LSPR. Then the mechanisms of LSPR effects on enhancing photodetectors' performance will be elucidated. In the next part, we will summarize the recent progress on photodetectors enhanced by LSPR effects in the past few years. Finally, we will present the existing challenges and the future opportunities in the field of LSPR enhanced photodetectors.

2 Physical mode of surface plasmon

Plasmon is a collective oscillation of electron gas with respect to the fixed positive ions in a metal under applied driving force. When excited by incident light, the plasmon is confined at the surface of metal structures, defined as a surface plasmon. According to the propagation length, surface plasmon excitation modes can be divided into SPPs and LSPRs [46, 47]. SPP is a transverse-magnetic surface wave that exists at the interface between a dielectric and a conductor with negative real permittivity. Under the SPPs mode, electrons will distribute as a rippling wave pattern in space due to the coupling of the electromagnetic field with the conductor's plasma [Fig. 2(a)]. However, SPPs mode is only excited under a special excitation setup, like a gold film-coated prism [48], to satisfy the momentum conservation and phase-matching conditions, limiting its use in low-dimensional photodetectors. Different from SPPs, LSPR is a non-propagating excitation of the conduction electrons that exists in the sub-wavelength metallic nanostructures, which could be coupled to the electromagnetic field [Fig. 2(b)] [48]. At the resonance frequency, the light can be confined at the nanoscale, resulting in an enhanced electromagnetic field. The enhancement factor is typically on the order of 10^2–10^3. Thus, LSPR mode provides a promising strategy for improving the device performance of low-dimensional photodetectors. In this section, we will derive the LSPR frequency equation from the Drude–Lorentz model and the dipole model, which are the fundamental theories for LSPR and served as guides for the development of plasmonic materials and devices.

2.1 Drude–Lorentz model

Drude–Lorentz model is a classical theory, which is used to describe the behavior of electrons in a solid material when subjected to an external electromagnetic field. Drude model assumes the electrons in a metal behaving like a gas of free particles moving through a lattice of positive ions. Lorentz oscillator model describes the response of electrons to an electromagnetic field. It regards the electrons as being bound to their atoms by springs and responding to the field with a characteristic resonant frequency. Thus, we derive the Drude–Lorentz model to define the interaction between free carriers of materials and the incident light. The motion equation of an electron in the material under an external electric field, while ignoring the lattice potential and electron–electron interactions, can be described as

$$m\ddot{\boldsymbol{x}} + m\gamma\dot{\boldsymbol{x}} = -e\boldsymbol{E}, \tag{1}$$

where m is the mass of the electron, $\dot{\boldsymbol{x}}$ and $\ddot{\boldsymbol{x}}$ are the first and second order derivatives of $\boldsymbol{x}$ (displacement of the electron), separately. The damping constant caused by electrons collisions is defined as $\gamma = 1/\tau$, τ is the relaxation of free electrons gas which is typically on the order of 10^{-14} s at room temperature. The function of $x(t)$ can be described as follows under driving field $E(t)$:

$$E(t) = E_0 e^{i\omega t}, \tag{2}$$

$$x(t) = \frac{e}{m(\omega^2 + i\gamma\omega)} \boldsymbol{E}(t). \tag{3}$$

E_0 and ω are the intensity and frequency of the external field, respectively. The combination of Eq. (3) and polarization formula $\boldsymbol{P} = -en\boldsymbol{x}$ can export complex dielectric function of material:

$$\varepsilon(\omega) = \varepsilon'(\omega) + i\varepsilon''(\omega), \tag{4}$$

$$\varepsilon' = \varepsilon_\infty - \frac{\omega_p^2}{\omega^2 + \gamma^2}, \tag{5}$$

$$\varepsilon'' = \frac{\omega_p^2 \gamma}{\omega(\omega + \gamma^2)}, \tag{6}$$

$$\omega_p = \sqrt{\frac{n_e e^2}{\varepsilon_0 m^*}}, \tag{7}$$

where ε' and ε'' represent the real and imaginary parts of the dielectric function, respectively. ε_∞ is the high-frequency dielectric constant of materials (usually $1 \leqslant \varepsilon_\infty \leqslant 10$). ω_p is defined as the plasma frequency of free electron gas, which plays a significant role in determining the frequency of the LSPR. n_e is the density of free carriers. M^* is the effective mass of carriers. Equations (4)–(7) are used to discribe the Drude–Lorentz model, illustrating the relationship between the incident light frequency and the dielectric function of materials. This is necessary for the two kinds of surface plasmon excitations which we will discuss in the next two parts.

2.2 Surface plasmon polariton

SPP is one of the surface plasmon excitations that exists at a planar interface of bulk materials with negative real permittivity. In this section, we will derive the propagation conditions of SPPs modes and showcase the applications based on SPPs photodetectors.

Figure 3(a) illustrates the propagation of SPPs wave along a metal-dielectric interface and the field energy decays exponentially in the z-axis, which means that SPPs wave is a kind of evanescent wave. Boundary condition requires the dielectric function of the metal and dielectric (air) for transverse magnetic (TM) mode incident light as follows:

$$\frac{k_1}{k_2} = -\frac{\varepsilon_1}{\varepsilon_2}. \tag{8}$$

$k_i \equiv k_{z,i}\,(i = 1, 2)$ is the z-direction propagation attenuation constant in the two media, which is a real positive number. So Eq. (8) requires $\mathrm{Re}[\varepsilon_1] < 0$ if $\varepsilon_2 > 0$. Similarly, for transverse electric (TE) mode, the boundary condition requires

$$A_1(k_1 + k_2) = 0. \tag{9}$$

According to Eq. (9), the condition can only be fulfilled when $A_1 = 0$. Therefore, no surface modes exist for TE polarization. Overall, SPP is always excited by TM wave and only exist under the conditions, in which the permittivity of one of the materials is negative and the other one is positive.

The dispersion relation of SPPs mode can be derived from Maxwell's equation and illustrated in Fig. 3(a),

$$k_{SPPs} = \frac{\omega}{c}\left(\frac{\varepsilon_1 \varepsilon_2}{\varepsilon_1 + \varepsilon_2}\right)^{\frac{1}{2}}. \tag{10}$$

k_{SPPs} is the SPP propagation constant [Fig. 3(b)]. Dispersion curve corresponds to the SPPs excitation ($\gamma = 0$) lying on the right hand of the propagating photon, indicating that the free-space photon has less momentum than SPPs mode at the same frequency [Fig. 3(a)]. So SPPs mode could not be excited by incident light directly due to the momentum mismatch. To break this mismatch, artificial coupling structures such as prism or grating are designed. Kretschmann [51] is the most widely used prism coupling structures at present [Fig. 3(b)]. The beam reflected at the interface between the metal and prism will give the metal an in-plane momentum of $k_x = k\sqrt{\varepsilon}\sin\theta$, which is sufficient to excite SPPs at the interface between metal and air. Utilizing this theoretical framework, SPPs photodetector has been designed and developed. Echtermeyer *et al.* [52] coupled graphene with a metal plasmonic gating to achieve 400% enhancement of responsivity. Seo *et al.* [53] engineered a photodetector based on SPPs by incorporating Ag nanowires (NW) with graphene. In this device, the SPPs propagate along the interface between the Ag NW and the glass substrate, while graphene serves as an ideal medium for detecting the evanescent electric field. In this review, the section on SPPs is merely an introductory overview, not the focal point of our discussion. Zhang *et al.* [54] gave a detail review about SPP, including the excitation progress, basic properties and recent publications.

2.3 Localized surface plasmon resonance

LSPR is another fundamental excitation of surface plasmon. When an electromagnetic field is applied to a metallic nanostructure with its size smaller than incident light, a collective oscillation of electrons occurs, resulting in a remarkable near-field enhancement and enhanced optical absorption at LSPR frequency. LSPR frequency is determined by multiple parameters, including the density of free electrons, the effective electron mass, size, geometry and distribution of the metal nanoparticles. We can deal with the optical response for subwavelength nanoparticles by quasi-static approximation, which regards the electromagnetic field as an electrostatic field due to the negligible phase change in nanoparticle's

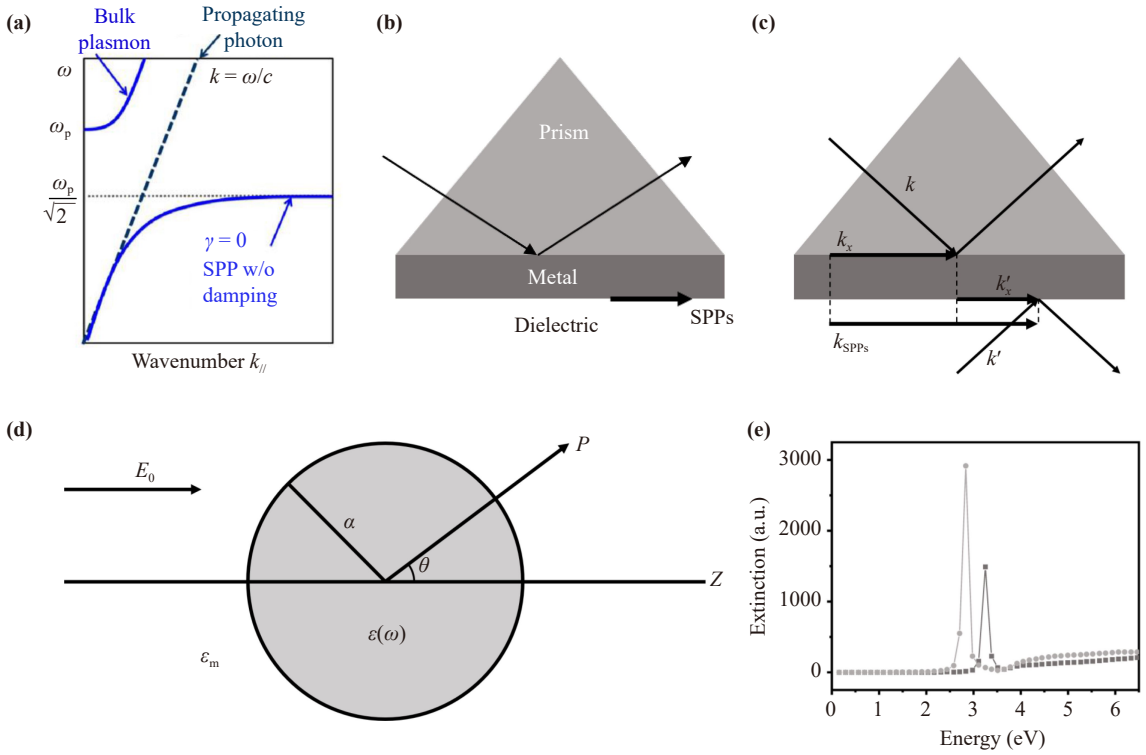

Fig. 3 **(a)** Dispersion relations for propagating photon (dashed navy line), bulk plasmons (top left blue branch) and SPPs on a metal-vacuum interface (bottom right blue branch) [49]. **(b)** Prism coupling of SPPs: Kretschmann configuration. **(c)** Illustration of momentum mismatch in Kretschmann configuration. **(d)** Schematic of a homogeneous nanosphere in an electrostaic field. **(e)** Extinction spectrum calculated via Eq. (12) for a sliver sphere (black curve) and a silica sphere (gray curve) in air [50]. (a) Reproduced from Ref. [49]. (b–e) Reproduced from Ref. [50].

spatial volume. In this section, we will discuss how to obtain the LSPR frequency and cross section in quasi-static approximation based on a homogeneous and isotropic nanosphere by electrodynamics [Fig. 3(d)].

Firstly, electric potential distribution can be deduced by solving Laplace equation $\nabla^2\Phi = 0$. The general solution for spherical symmetry field can be described by Legendre Polynomials $P_l(\cos\theta)$ [55],

$$\Phi(r,\theta) = \sum_{l=0}^{\infty}\left[A_l r^l + B_l r^{-(l+1)}\right] P_l(\cos\theta), \tag{11}$$

where l is the order of Legendre Polynomials, θ is the angular between vector $\boldsymbol{P}$ and z-axis. From the boundary condition at $r \to \infty$ and $r = a$, where a is the radius of the sphere. So electric potential inside and outside are determined separately:

$$\Phi_{in} = -\frac{3\varepsilon_m}{\varepsilon+2\varepsilon_m} E_0 r\cos\theta, \tag{12}$$

$$\Phi_{out} = -E_0 r\cos\theta + \frac{\varepsilon-\varepsilon_m}{\varepsilon+2\varepsilon_m} E_0 a^3 \frac{\cos\theta}{r^2}. \tag{13}$$

Φ_{out} is the superposition of the applied field and dipole field excited in the nanosphere. $\varepsilon(\omega)$ and ε_m are the dielectric function of particle and dielectric, respectively. E_0 is the magnitude of applied electric field. Equation (13) can be rewritten by dipole moment $\boldsymbol{p}$:

$$\Phi_{out} = -E_0 r\cos\theta + \frac{\boldsymbol{p}\cdot\boldsymbol{r}}{4\pi\varepsilon_0\varepsilon_m r^3}, \tag{14}$$

$$\boldsymbol{p} = 4\pi\varepsilon_0\varepsilon_m a^3 \frac{\varepsilon-\varepsilon_m}{\varepsilon+2\varepsilon_m}\boldsymbol{E}_0. \tag{15}$$

Therefore, the polarizability α is defined by the relationship between dipole moment and electric field $\boldsymbol{p} = \varepsilon_0\varepsilon_m\alpha\boldsymbol{E}_0$:

$$\alpha = 4\pi a^3 \frac{\varepsilon-\varepsilon_m}{\varepsilon+2\varepsilon_m}. \tag{16}$$

It is obvious that α tends to be infinite when $\mathrm{Re}[\varepsilon(\omega)] = -2\varepsilon_m$, representing a resonance, which is called Fröhlich condition. Hence, we can deduce the LSPR resonance frequency (ω_{lsp}) by combining Eq. (16) and Eq. (5):

$$\omega_{lsp} = \sqrt{\frac{n_e e^2}{\varepsilon_0 m^*(\varepsilon_\infty+2\varepsilon_m)} - \gamma^2}. \tag{17}$$

Equation (17) illustrated that the LSPR frequency can be adjusted by controlling the electron density. This implies that the LSPR frequency can be manipulated by adjusting the n_e of materials, which represents the most

common tuning methods for semiconductor plasmonic materials. Besides, the minimum carrier concentration limitation existed for keeping the materials with negative permittivity:

$$n_{\min} = \frac{\varepsilon_\infty \varepsilon_0 m^*}{e^2}\left(\omega_c^2 + \gamma^2\right). \tag{18}$$

Cross section is widely applied to express the optical properties of nanoparticles. Plasmonic nanoparticles have a larger scattering cross section than their real spatial volumes, which is the key for breaking the diffraction limits. The scattering cross section C_{sca} and absorption cross section C_{abs} for the nanosphere can be expressed as follows:

$$C_{sca} = \frac{k^4}{6\pi}|\alpha|^2 = \frac{8\pi}{3}k^4 a^6 \left|\frac{\varepsilon - \varepsilon_m}{\varepsilon + 2\varepsilon_m}\right|^2, \tag{19}$$

$$C_{abs} = k\mathrm{Im}\left[\alpha\right] = 4\pi k a^3 \mathrm{Im}\left[\frac{\varepsilon - \varepsilon_m}{\varepsilon + 2\varepsilon_m}\right], \tag{20}$$

$$C_{ext} = 9\frac{\omega}{c}\varepsilon_m^{3/2} V \frac{{\varepsilon_1}''}{\left({\varepsilon_1}' + 2\varepsilon_m\right)^2 + {\varepsilon_1}''^2}, \tag{21}$$

where C_{ext} is the total excitation cross section, which is equal to $C_{sca} + C_{abs}$. Since $C_{sca} \propto a^6$ and $C_{abs} \propto a^3$, light scattering effect is dominant in larger NPs, while absorption effect is dominant for smaller NPs conversely. The typical extinction spectra of sliver and silica nanospheres in air calculated by Eq. (21) are shown in Fig. 3(e) [50].

All in all, LSPR mode excited in quasi-static particles can be interpreted as an electric dipole. Fröhlich condition is the frequency requirement for incident light to achieve the highest resonance peak. Additionally, Mie's theory is valid for describing particles with larger dimensions where the quasi-static approximate is not effective. For a more complex nanoparticle structures like cubes, core-shell or other geometries, the calculation of cross-section would be more complicated and abstract. Some numerical methods have been developed with notable examples including the discrete dipole approximation (DDA) [56], the finite difference time domain (FDTD) method [57], and the finite element method (FEM) [58].

3 Plasmonic materials and tunability of LSPR frequency

Based on the introduction in Section 2, we have gained an understanding of the generation principles and related theoretical foundations of LSPR. Building upon this theoretical foundation, various plasmonic materials and corresponding modulation methods have emerged. In this section, we primarily focus on the modulation methods and influencing factors of LSPR peaks in metallic and semiconductor plasmonic materials. We summarize the differences in LSPR peaks of metallic nanoparticles with different shapes and analyze the reasons for the generation of different peaks theoretically. For semiconductor nanocrystals, we summarize different carrier modulation methods such as doping, chemical post-treatment, and photo-doping, which lay the foundation for better understanding of plasmonic materials. The corresponding the fabrication method will also be introduced.

According to Eq. (17), the localized surface plasmon frequency is proportional to the density of free carriers. Hence, adjusting the electron density is the main approach to tuning the LSPR frequency of plasmonic materials. Noble metals, such as gold, silver, copper and aluminum, are the most applied plasmonic materials with LSPR frequency ranging from UV to visible region because of their high free electron density of ~10^{23} cm^{-3}. The plasmonic properties of noble metals can be engineered by controlling their size, geometry, crystal structure, composition, arrangement and surrounding medium. For the particles with their size much smaller than the wavelength of incident light, the LSPR peak tends to be in the longer wavelength range with size increasing due to the better charge separation. Evanoff *et al.* [59] reported the size dependent LSPR peaks in silver nanospheres and nanotubes [Fig. 4(a)]. When the particle size is comparable to the resonance wavelength, the uniformed electric field distribution along with the spatial volume of particles leads to the excitation of multipolar plasmon oscillation and multi LSPR peaks. The geometry of metal nanostructure also has a strong effect on LSPR properties. Rycenga *et al.* [60] summarized the experimental and calculated extinction spectra of different Ag nanostructure. Calculated results based on Mie theory for 40 nm Ag nanospheres were almost the same as experimental results, in which the peak wavenumber and intensity fit the Mie simulation very well. While the calculated results based on DDA method for nanocube, nanooctahedron or bipyramid were not as good as nanosphere, in which some shoulder peaks were missed compared to experiment result. Amendola *et al.* [61] summarized the LSPR spectrum of gold nanoparticles with different geometries, including nanospheres, nanorods, core-shells, nanotriangles, nanocubes, etc. [Figs. 4(b)–(d)]. Wiley *et al.* [62] calculated the extinction spectrum of silver nanoparticles with different shapes by discrete dipole approximation (DDA) method and concluded that LSPR peaks tended to be multi-peaks accompanying by the decrease of shape symmetry. Link *et al.* [63] reported the absorption spectra of gold nanorods with an aspect ratio from 2.6 to 3.6 [Fig. 4(e)]. The gold nanorods exhibited two LSPR peaks simultaneously which were transverse mode at the short axis and longitudinal mode at the long axis.

Moreover, they also demonstrated that longer oscillation displacement at the long axis leaded to the lower resonance

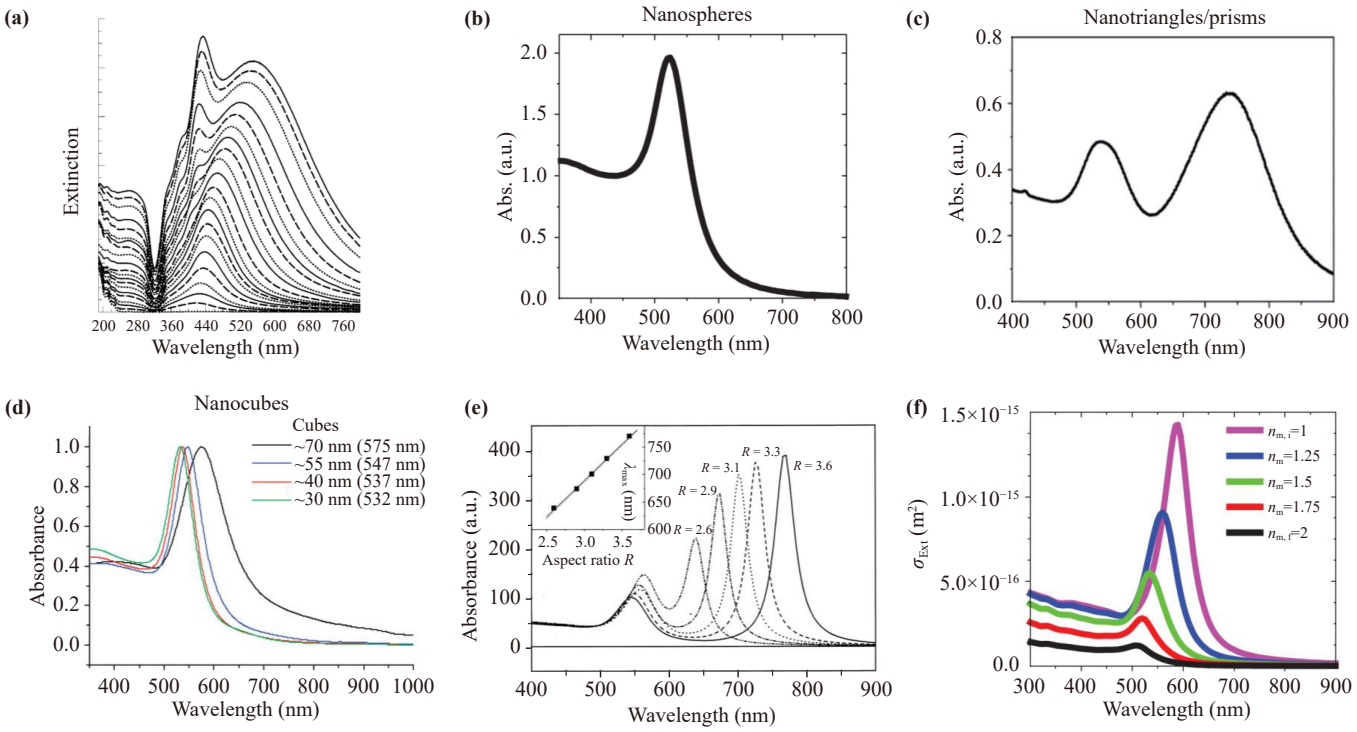

Fig. 4 **(a)** Extinction spectra of silver nanoparticles of 20 difference diameters (from 6 nm to beyond 70 nm). And the peak shift rapidly to longer wavelength as the particles size increases. **(b–d)** Optical extinction spectrum of Au NPs (nanospheres, nanotriangles and nanocubes). **(e)** The calculated absorption spectrum of elongated ellipsoids with varying aspect R which is defined as A/B. A and B are the long axis and short axis separately. Inset shows the function of resonance maximum wavelength λ_{max} and aspect ratio R [63]. **(f)** Extinction cross section of a 20 nm Au NP in a non-absorbing media with the refractive index increasing from $n_{m,i} = 1$ to $n_{m,f} = 2$, calculated by Mie model [61]. (a) Reproduced from Ref. [59]. (b–d) Reproduced from Ref. [61]. (e) Reproduced from Ref. [63]. (f) Reproduced from Ref. [70].

frequency and the resonance wavelength was proportional to the aspect ratio. Zeng *et al.* [64] reported an obvious blue-shift of LSPR peaks of Ag nanoplates from triangular to sphere with the corner sharpness decreasing, which was due to the dramatic near-field enhancement and high increasing factor by sharp corner. Alloying or constructing the core/shell structures based on metals could also tune the LSPR frequency. Ag-Au [65], Ag-Pt [66], and Ag-Pd [67] alloyed metals exhibited obvious different plasmonic properties from pure Ag nanocrystals. The LSPR peak can be red-shifted by controlling the molar ratio, from 440 nm for pure Ag nanocrystals to ~700 nm for Ag-Au, ~732 nm for Ag-Pt, and ~670 nm for Ag-Pd. Au@Ag core–shell structure showed two distinct LSPR peaks, corresponding to the intrinsic peaks of core and shell materials, separately. And the peak intensity was primarily dependent on the shell thickness [68, 69]. Besides, the dielectric constant ε_m of the surrounding medium could affect the LSPR frequency according to Eq. (17). The LSPR peak would red-shift to longer wavelength with increasing ε_m [Fig. 4(f)] [70].

Other metallic material, such as Al, also exhibits similar LSPR tuning capabilities as Ag. The LSPR of Al has been demonstrated in various nanostructures, like spheres [71], triangles [72], discs [73, 74], and rods [75]. Due to its higher d-band energy level, Al with nanostructures can exhibit plasmon resonance extending into the ultraviolet region. Additionally, owing to its higher electron density and the self-forming oxide protective layer, Al with lower cost, is considered as the primary choice for plasmonic applications, especially for mass productions. Stöckli *et al.* [76] simulated the surface plasmon energy for Al nanospheres with varying ratio. Taguchi *et al.* [77] controlled the size of deposited Al nanotriangles by adjusting the distance between the nanosphere masks using microwave heating, achieving tunable LSPR peak positions in the range of 260 to 340 nm. Knight *et al.* [78] also found two resonance mode in Al nanorods with transverse mode showing higher energy. Furthermore, they provided the scattering spectra of Al nanorods of different lengths, showing that the energy of the longitudinal mode decreased with the length of the nanorod, while the energy of the transverse mode remained almost unchanged.

The preparation methods of metal plasmonic materials typically involve physical techniques such as photolithography, deposition, etching, and annealing. In this case, the fabrication and integration of the material are carried out simultaneously. As shown in Fig. 5(a),

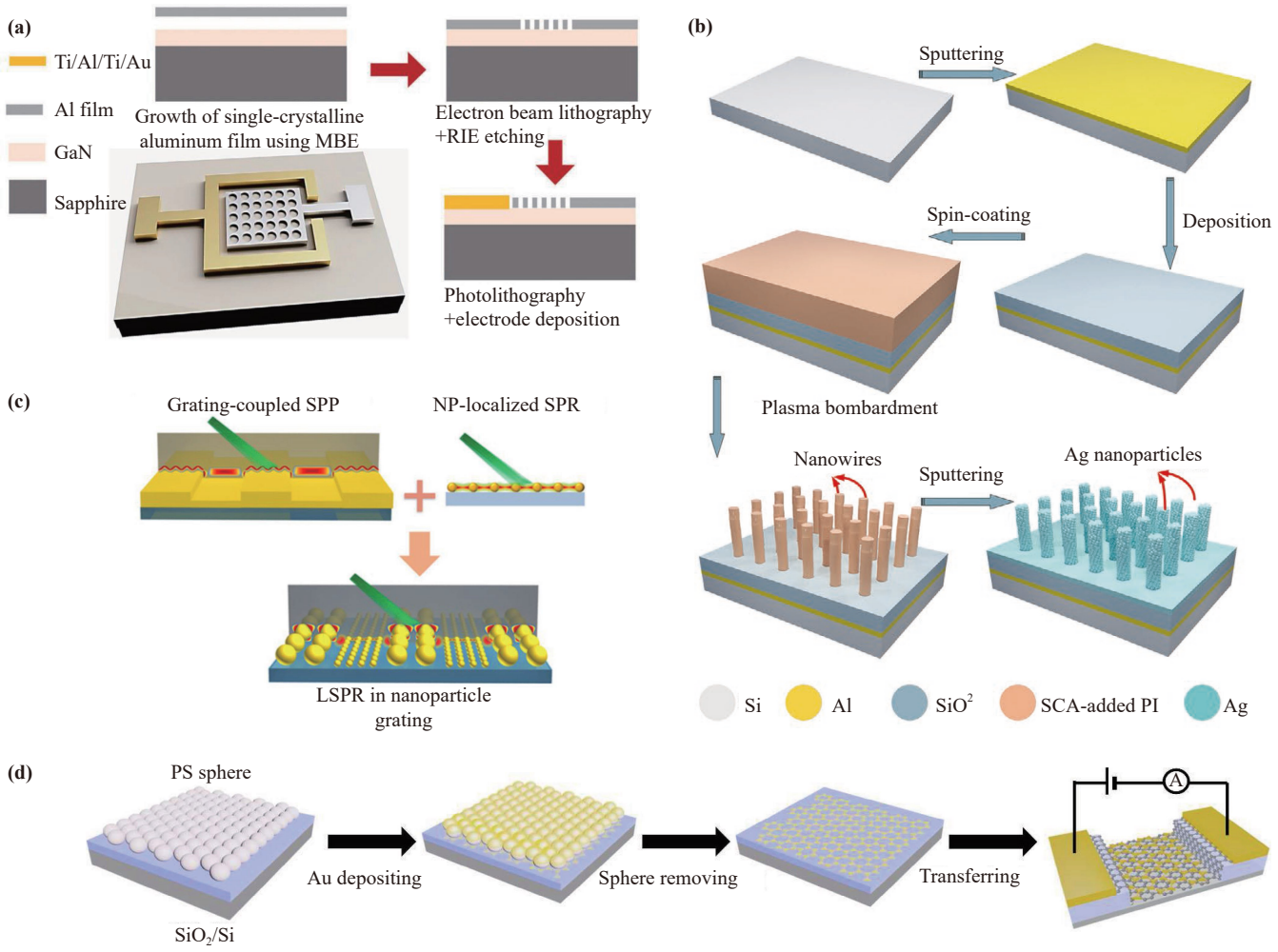

Fig. 5 **(a)** Fabrication process of Al nanoholes GaN UV photodetector. **(b)** Fabrication process of the broadband Ag-QNF absorber. **(c)** Fabrication process of Au-MoS_2 photodetector. **(d)** Fabrication process of Au NP array graphene SWIR photodetector. (a) Reproduced from Ref. [79]. (b) Reproduced from Ref. [80]. (c) Reproduced from Ref. [81]. (d) Reproduced from Ref. [82].

Dubey *et al.* [79] utilized molecular beam epitaxy (MBE) for growth of Al thin film, followed by electron beam lithography (EBL), reactive ion etching (RIE), and metal deposition to create a layer of circular Al plasmonic structures on a GaN absorption layer. Li *et al.* [80] designed an Ag-quasi-ordered nanoforest structure [Fig. 5(b)], where the required materials were first deposited as thin films using methods such as deposition and spin-coating. Subsequently, the polyimide (PI) nanoforest structure was prepared through plasma bombardment, followed by attaching Ag nanoparticles onto the PI nanoforest surface via sputtering. To achieve periodic arrangement of Au nanoparticles of different sizes, Li *et al.* [81] initially deposited Au thin films of various thicknesses on SiO_2, then annealed the Au films to form Au nanoparticles of different sizes, thus realizing the arrangement mode of periodic nanoparticle gating [Fig. 5(c)]. Chen *et al.* [82] utilized polystyrene (PS) spheres as masks and further employed Au deposition methods to achieve the fabrication of a triangle-like Au NPs array [Fig. 5(d)]. The shape and structure of plasmonic structures can be well controlled using physical methods. Combined with FDTD simulations, specific patterns can be designed to achieve a strong surface electromagnetic field enhancement effect. Different from plasmonic metals, LSPR of semiconductors can be generated by either holes in the valence band or electrons in the conductive band. The typical plasmonic semiconductor materials include metal oxides (ZnO [83, 84], In_2O_3 [85], CdO [86], MoO_2 [87] ,WO_3 [88], etc.), copper chalcogenides ($Cu_{2-x}S$ [89], CuSe [90], Cu_2SSe_x [91], etc.) and doped silicon [92]. Due to the relatively low carrier density of 10^{18} to 10^{22} cm^{-3}, semiconductors usually exhibit an LSPR frequency in the infrared region. Adjusting the doping type and the density are general strategies to tune the LSPR frequency of semiconductors. Over the past decades, various techniques, such as induced synthetically via chemical doping or post synthetically

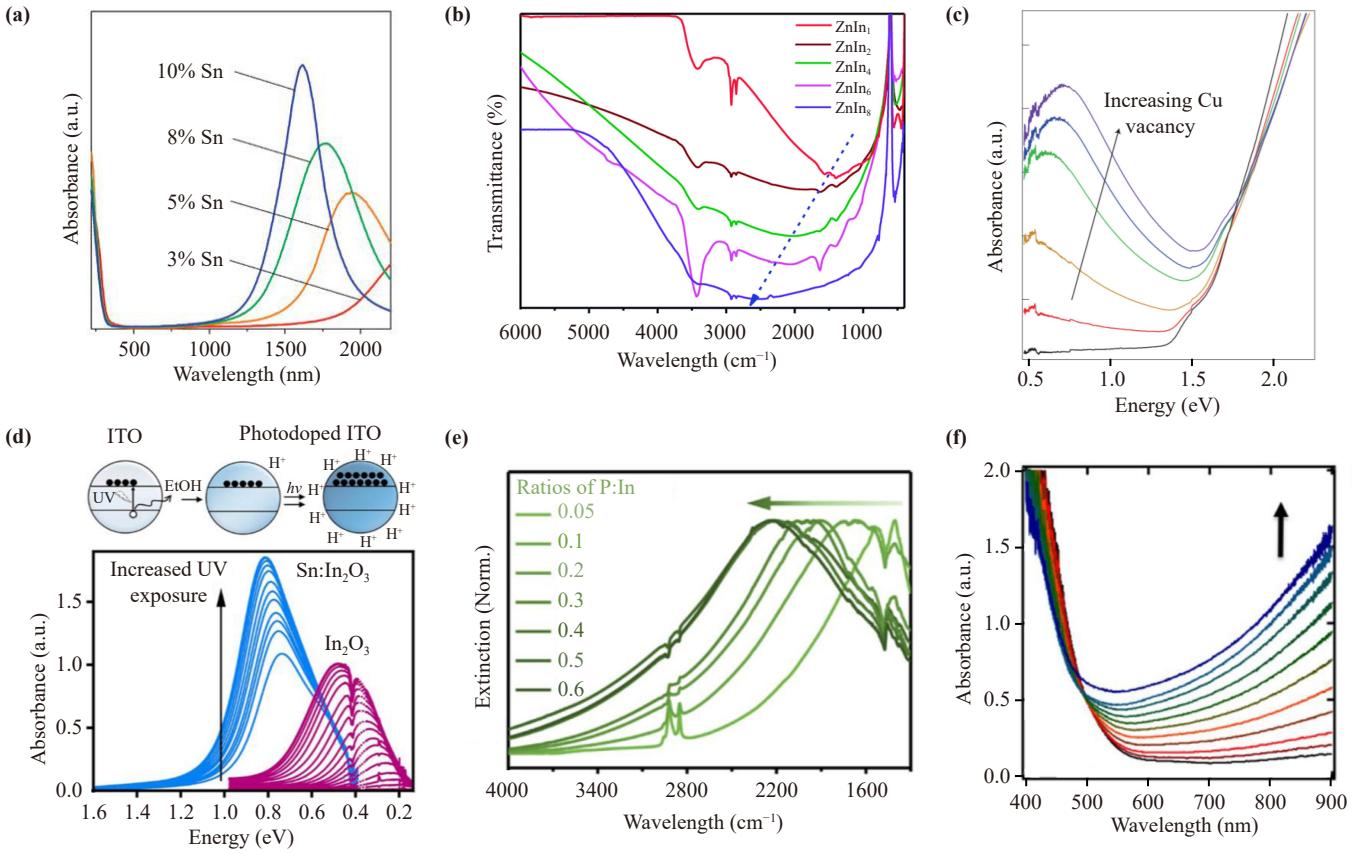

Fig. 6 **(a)** UV-Vis-NIR absorption spectra of ITO NPs doped with 3%–10% Sn. **(b)** FTIR transmission spectrum of ZnO NC with varying In doping concentrations (from 1% to 8%). **(c)** Absorbance spectrum of Cu_2S nanorods. The stoichiometric Cu_2S nanorods (black line) without NIR LSPR absorbance. **(d)** The top part illustrates the photodoped process in ITO nanocrystals. The bottom is the absorbance spectrum of In_2O_3 and 9% Sn-doped In_2O_3 before and after photodoping. The arrow reveals photodoping concentration increases with increasing UV exposure. **(e)** Extinction spectra of P-In_2O_3 nanocrystals with P:In ratio from 0.05 to 0.6. **(f)** Absorption spectra of ZnO NCs with 20 equiv Cp^*_2Co. (a) Reproduced from Ref. [95]. (b) Reproduced from Ref. [94]. (c) Reproduced from Ref. [89]. (d) Reproduced from Ref. [98]. (e) Reproduced from Ref. [100]. (f) Reproduced from Ref. [101].

via chemical redox reactions and photochemical reactions, have been explored to modulate the LSPR frequency of semiconductors and significant advances have been achieved.

Aliovalent doping, a major method of adjusting the carrier density, has been developed in metal oxide, such as tin-doped indium oxide (Sn:In_2O_3), aluminum-doped zinc oxide (Al:ZnO) [93], indium-doped zinc oxide (In:ZnO) [94], in which the doped ion serves as an electron donor in crystal structure to influence the free carrier density. Kanehara *et al.* [95] reported that the LSPR peak of ITO (Sn:In_2O_3) nanocrystals could be tuned from 1626 to 1940 nm by increasing the Sn-doped concentration [Fig. 6(a)]. Similarly, Ghosh *et al.* [94] reported the tunable plasmon resonance of In-doped ZnO nanocrystals in by adjusting the doped In concentration [Fig. 6(b)]. Self-doping by changing stoichiometry to generate vacancies is another way to adjust the carrier density in some metal oxide and copper chalcogenide. Su *et al.* [96] achieved tunable LSPR peaks of $W_{18}O_{49}$ nanorods by evaporating tungsten bulk in an oxygen-deficient environment. Red-shift of the LSPR peak accompanied by decreased plasmon intensity was observed as oxygen content decreased. Lee *et al.* [97] developed a pyrolysis method for synthesizing MoO_{3-x} nanocrystals, exhibiting LSPR peaks from 620 to 950 nm. The mechanism of tuning LSPR frequency is similar for copper chalcogenides due to the copper vacancies. Luther *et al.* [89] excited the LSPR peak of $Cu_{2-x}S$ nanocrystals at the NIR region by exposing it to an oxygen atmosphere, which leads to the copper vacancy generation [Fig. 6(c)]. Copper vacancies increase the LSPR intensity and cause the peak blue-shifts with longer exposure time. Photodoping strategy can increase the conductive electron by suppressing the photo-generated electron–hole pair combination by removing the photo-generated hole with a hole-scavenger. Schimpf *et al.* [98] reported an ITO nanocrystal with LSPR peak excited by photodoping. The intensity of the ITO absorbance peak increased gradually and shifted to the high-energy region

under rigorously anaerobic conditions with UV illumination [Fig. 6(d)]. Besides, Jain's group [99] realized ZnO nanocrystal LSPR dynamic switching in the IR region by photo-excitation charging and redox discharging.

The free carriers in semiconductors can also be induced post synthetically via photochemical reactions or chemical redox reactions, which have no effects on the element composition. Du *et al.* [100] demonstrated a general and simple post-synthetic method for the generating of plasmonic oxide nanocrystals via surface anchoring of redox-active phosphorus species. A redox reaction generated free electrons in the oxide nanocrystals, accompanied by the valance-state changes of the surface-anchored phosphorus species from −III to +V. The resulting nanocrystals showed tunable plasmon resonance peaks in the near-infrared or mid-infrared regime [Fig. 6(e)]. In this study, Drude model was employed to fit the LSPR peak of P-In_2O_3, and the calculated results show strong consistence with experimental results. Valdez *et al.* [101] achieved tunable carrier density of ZnO nanocrystal by exposing the ZnO nanocrystal to an aprotic solvent with excess one-electron reductant agent Cp^*_2Co (Cp^* = pentamethylcyclopentadienyl), the ZnO nanocrystals were reduced by Cp^*_2Co when protons were added. The ZnO nanocrystal are reduced by up 1−3 electrons per NC, and this number could be increased to 15 in the presence of acid. The absorbance of ZnO in NIR region is increased after 10 μL aliquots of $[H(Et_2O)_2^+][BAr^{F-}_4]$ treatment [Fig. 6(f)]. Milliron's group [85] achieved a shift more than 1200 nm in the plasmon wavelength of ITO nanocrystals film by post synthetic electrochemical modulation. This bias-induced shift was much stronger than previous results observed in other system, which may be caused by less surface defect sites in ITO film.

Since the synthesis of semiconductor nanocrystals is typically based on wet chemistry methods, the resulting plasmonic semiconductor nanocrystals possess excellent solution processability, thus they can be transferred to the desired device surface with liquid phase. Lu *et al.* [102] constructed an ITO NPs@SLG/Ge NNs array NIR photodetector, where heavily doped ITO nanoparticles were synthesized via a reflux method in oleylamine and then transferred to the surface of monolayer graphene through spin-coating, achieving LSPR in the infrared spectrum. Ni *et al.* [103] developed a broadband photodetector using B-doped Si QDs@graphene, where colloidal Si QDs were also transferred to the graphene surface via spin-coating. It should be noted that for the spin-coating transfer method, the concentration of nanocrystal solution and rotation speed are needed to be controlled within an appropriate range to ensure the density of nanocrystals film.

LSPR properties adjustment for semiconductor nanocrystal is primarily focused on the controlling carrier density according to Eq. (17). The traditional aliovalent doping and self-doping synthetic strategies, i.e., synthetically via chemical doping, mainly rely on balancing reactivity between the precursors for the dopants and the host semiconductors, which is always restrictive. Besides, these methods are either through a high-expensive process or yield plasmonic nanocrystals with low stability. Photodoping offers a non-destructive carrier density modulation in nanocrystals. However, the limitation of photodoping is that only n-type doped is permitted. Post-synthetic chemical redox reactions bypass the challenges associated with the chemical doping strategy and can make full use of the rich synthetic chemistry developed for colloidal oxide nanocrystals. Thus, this post-synthetic strategy holds the promise of generating plasmonic semiconductors with tight control over size, shape and free carrier densities.

4 Enhancement mechanism of LSPR photodetectors

After introducing the physical model and material basis of LSPR, this section focuses on discussing the mechanism of LSPR-enhanced photodetectors. Within the field, there are two common understandings regarding the reasons for the performance enhancement of LSPR-based photodetectors: near-field enhancement and hot-electron injection. This section summarizes explanations of these two enhanced mechanisms and the current research on improving the efficiency of hot-electron injection, which is crucial for enhancing the performance of LSPR-based devices.

A main application of LSPR is to enhance the performance of photodetectors. For a photodetector, there are generally three processes for detecting optical signals: (i) generation of hot carriers by excitation of incident light; (ii) separation of photogenerated carriers; and (iii) transportation and extraction of separated carriers for electric signals output. The enhanced performance of photodetectors by LSPR is mainly through two mechanisms: (i) near-field enhancement and (ii) plasmon-induced hot electron injection. Plasmonic nanomaterials act like an optical antenna at the resonance frequency, which has an excellent light confine effect and achieves near-field enhancement, making absorption of incident light more effective and exciting more intrinsic electron–hole pairs. The plasmon-induced hot electron effect is particularly complex and uncontrollable, which is, however, promising for LSPR enhanced photodetectors. The plasmonic nanomaterials can absorb light by intraband excitation, and the plasmon-induced hot electron could cross the Schottky barrier and inject into absorption layer to form an extra photocurrent. In this part, we will discuss the above two enhancement mechanisms of LSPR photodetectors in details.

4.1 Near-field enhancement

Near-field enhancement (NFE) means that the electromagnetic field density can be enhanced by orders of magnitude on the surface of plasmonic nanostructures, which is induced by near-field electronic polarization. The near-field effect is a major topic in the field of surface plasmon, which is explored in various optical phenomena, such as Raman scattering, fluorescence and other nonlinear optical effects. The enhancement factors are influenced by many parameters, such as geometry [104–107], interval distance [108, 109], and carrier concentration [105]. Photon-induced near-field electron spectroscopy (PINEM) and finite-different time-domain method (FDTD) are often used to confirm the NFE around plasmonic nanostructures both experimentally and theoretically. Meunier *et al.* [110] calculated the electric field enhancement distribution of Au nanoparticles, nanoshells and nanorods [Fig. 7(a)]. They achieved a maximum field enhancement of 77.1 at the tips of the nanorod. Yurtsever *et al.* [111] developed PINEM technique for space-time visualization of the near-field, which combined a laser pump with ultrafast electron microscopic. Figure 7(b) showed the enhanced near-field of two separated Ag NPs in two polarizations with PINEM. The PINEM technique offered an effective measurement to observe the nanoparticles' near-fields directly, which may promise a range of applications. Dong *et al.* [112] simulated the electric field enhancement of Au NPs arrays above the $CsPbBr_3$ photodetector of 532 nm and they provided the NFE map in three planes [Fig. 7(c)]. Atwater *et al.* [113] showed a standard NFE map of a 25 nm Au nanoparticle embedded in a medium with an index of 1.5 under 850 nm incident light. $|E|^2 > 10$ could be realized at the edge of the nanoparticle. Moreover, ITO, which contains conduction-band electrons is the most widely used transparent conducting oxide in the photoelectric field. The enhancement factors of ITO nanocrystals were typically about 10–35 for nanospheres [114] and 150–160 for nanorods [104]. Milliron's group [115] realized more than 400 NFE for cerium doped indium oxide (FITO) nanocubes. Kim *et al.* [107] studied the influence of crystalline anisotropies for plasmonic $Cs:WO_3$ nanocrystals and gave a simulation in longitudinal and transverse modes. The near-field intensity map illustrated that more than 400-fold enhancement was achieved.

4.2 Plasmon induced hot electron

As mentioned above, plasmonic nanoparticles can absorb the energy of an electromagnetic field and generate a strong resonance at LSPR frequency as a surface plasmon. However, the lifetime of surface plasmons is finite, as the plasmon resonance will either decay radiatively by re-emitting a photon [116] or non-radiatively by creating a hole–electron pair [117–119] [Fig. 8(a)]. The non-radiative decay process transfers the light energy to the excess kinetic energy of electrons and excite electrons from occupied levels above the Fermi level. The excited electrons are called hot electrons [120, 122–126]. Hot electrons play an important role in LSPR PD because the energy they possess has a probability to escape from the nanoparticle and directly inject into the conduction band of adjacent semiconductor layer across the Schottky junction [127–130] or tunnel-barrier [131, 132] at the interface. Thus, the photodetector could harvest the photon with energy below the semiconductor band gap in this approach, increasing the photocurrent.

The hot-electron injection process can be described in four steps: Firstly, incident light excites the surface plasmon and the energy is transferred as the kinetic energy to electrons to support collective oscillation. Then, the surface plasmon decays non-radiatively, mainly through the Landau damping [133], with energy transferred from electrons' collective resonance to induced hot electrons in less than 100 fs. After that, some hot electrons will quickly redistribute their energy by electron–electron scattering, such as Auger transitions [134], electron–phonon scattering process and electron-defect scattering. The redistribution process is called carrier relaxation and the relaxation time τ_{el} is about 100 fs to 1 ps. Finally, part of the hot electrons will transfer to the metal and semiconductor interface and pass across the interface when the kinetic energy is higher than the barrier energy Φ_B and tangential momentum continuity conditions are satisfied. As Fig. 8(d) illustrated, only electron with momenta in the angle Ω can pass across the interface barrier. Due to these limitations, the efficiency of electron harvest is relatively low. Au and Ag are the most widely used noble metals in plasmonic structure because of their relative low scattering rate of free electrons, resulting in lower loss compared to other metals. Khurgin *et al.* [135] discussed using semiconductors or polar dielectrics to improve the efficiency of electrons harvest. Size and surface ligands of metal nanocrystals also affect the efficiency of the transfer process [136, 137]. Furube and Du's group [138–140] used ultrafast visible-pump/infrared-probe femtosecond transient absorption spectroscopy to characterize the plasmon-induced hot electron process in Au nanoparticle-TiO_2 system and quantified the efficiency was ~40% under 550 nm excitation. Compared to metal plasmonic structures, in which the transferred hot carriers typically undergo a rapid recombination back to the metal [k_{rec} in Figs. 8(e) and (f)], semiconductor plasmonic structures exhibit a different hot carrier transfer process. This recombination process is being suppressed in semiconductor plasmonic structures due to the presence of bandgap and band-bending. Liu *et al.* [141]'s systematic study, employing first-principles calculations and Monte Carlo simulations, demonstrates that TiN exhibits significant advantages in both the generation (high density of low-energy hot electrons)

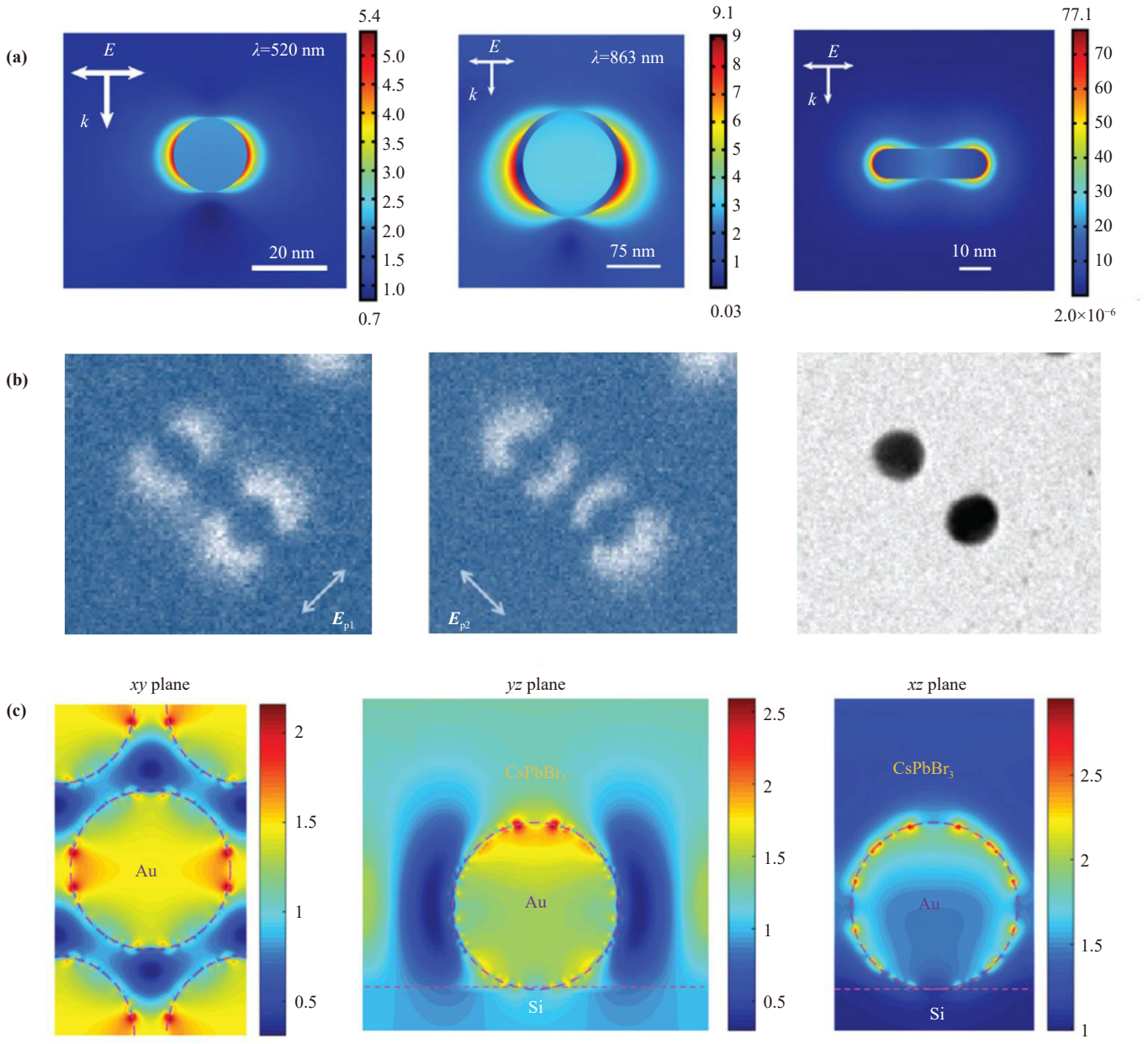

Fig. 7 **(a)** Electric field enhancement distribution around a D = 20 nm Au NP irradiated at plasmon frequency (λ = 520 nm), a 75 nm outer radius/65 nm inner radius SiO_2/Au NS at plasmon frequency (λ = 863 nm) and a 10 nm × 41 nm Au NR. **(b)** PINEM images of two close-by silver particles for two polarizations. The particles are separated by 70 nm (edge-to-edge). **(c)** FDTD simulation of Au NP arrays on $CsPbBr_3$ layer in three planes. (a) Reproduced from Ref. [110]. (b) Reproduced from Ref. [111]. (c) Reproduced from Ref. [112].

and transport (long lifetime and mean free path) of hot carriers. Furthermore, further device simulations indicate that high hot-carrier injection efficiency can be achieved in core/shell cylindrical TiN/TiO_2 structures. Yang *et al.* [142] facilitated a plasmonic p–n heterojunction ($Cu_{2-x}Se$–CdSe) in the near-IR excitation (1.1 eV) and observed a ~130 ps lifetime of the transferred electrons [Fig. 8(g)], which was two orders of magnitude longer than that in metal plasmonic structure-semiconductor counterparts.

Generation of plasmon-induced hot carrier is a complex process that is difficult to influence. In the past decade, great efforts have been made to gain a deep understanding of its physical essence. Govorov *et al.* [143] developed a theoretical model to estimate the hot carrier distribution based on the equation of density matrix motion and evaluated the injection efficiency of a plasmonic nanostructure. The researchers also showed that the energy of hot electrons varied according to the size of the nanoparticles. Nanoparticles with a width of 10–20 nm were found to generate hot carriers with high excitation energy. Manjavacas *et al.* [144] developed a

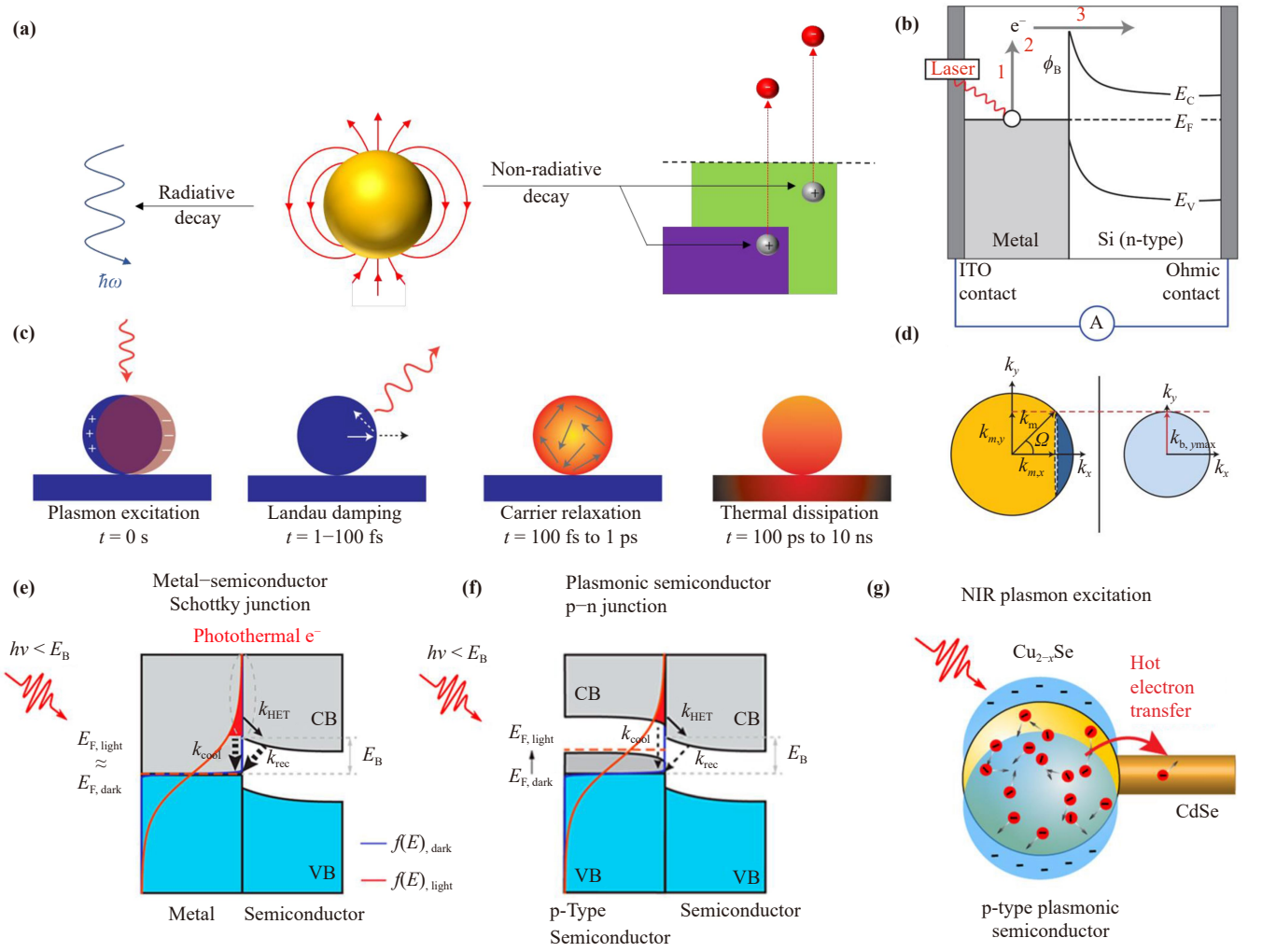

Fig. 8 **(a)** Two different decay mechanisms in during the surface plasmon. **(b)** Three steps in hot-electron injection process in a Schottky detector [120]. **(c)** Four steps in non-radiative decay process of surface plasmon. **(d)** Constant energy contours in metal (left)/barrier (right) region [121]. k_m is the hot electron momentum in the metal, Ω is the allowed maximum angle that still satisfied the conservation of momentum. **(e)** Band structure of a plasmonic metal–semiconductor Schottky junction. **(f)** Band structure of a plasmonic semiconductor–semiconductor Schottky junction. **(g)** Schematic of plasmon excitation process in $Cu_{2-x}Se$–CdSe system. (b) Reproduced from Ref. [120]. (c) Reproduced from Ref. [117]. (d) Reproduced from Ref. [134]. (e–g) Reproduced from Ref. [142].

theoretical framework describing the factors that influence the hot carrier generation rate induced by plasmon decay. They regarded the conduction electrons in metallic as free particles in a finite potential well [Fig. 9(a)] and analyzed the plasmon-induced dynamic using Fermi's golden rule. In this work, the authors revealed that both number of hot electrons generated per unit time and the efficiency (FoM) of the carrier generation depend on the hot carrier lifetime τ and particle size [Figs. 9(b, c)]. The FoM $\mathcal{N}_e(\varepsilon)$ is defined as the number of hot electrons possessing energy larger than a certain threshold ε compared to the Fermi level. However, the material types and interband transitions in noble metal were neglected in this paper. Sundararaman *et al.* [145] demonstrated the impacts of electronic band structures and nanoparticle geometries on carrier energy distributions. They used first-principles density function theory (DFT) to calculate the plasmonic hot-carrier energy and momentum-direction distribution in metals, including gold, aluminum, silver, and copper, based on a quantized plasmon model [Fig. 9(d)]. Only aluminum showed the electric field orientation dependence on electron and hole distributions along the x direction. Ranno *et al.* [146] developed an approach to promise bimetallic core-shell nanoparticles and gave the hot-carriers generation rates in alkali-metal core and a transition-metal shell system. Furthermore, Bernardi *et al.* [147] carried out ab initio calculation of hot electrons in GaAs with diamond structure by DFT and many-body perturbation theory to resolve the e–ph scattering problem. Their calculation

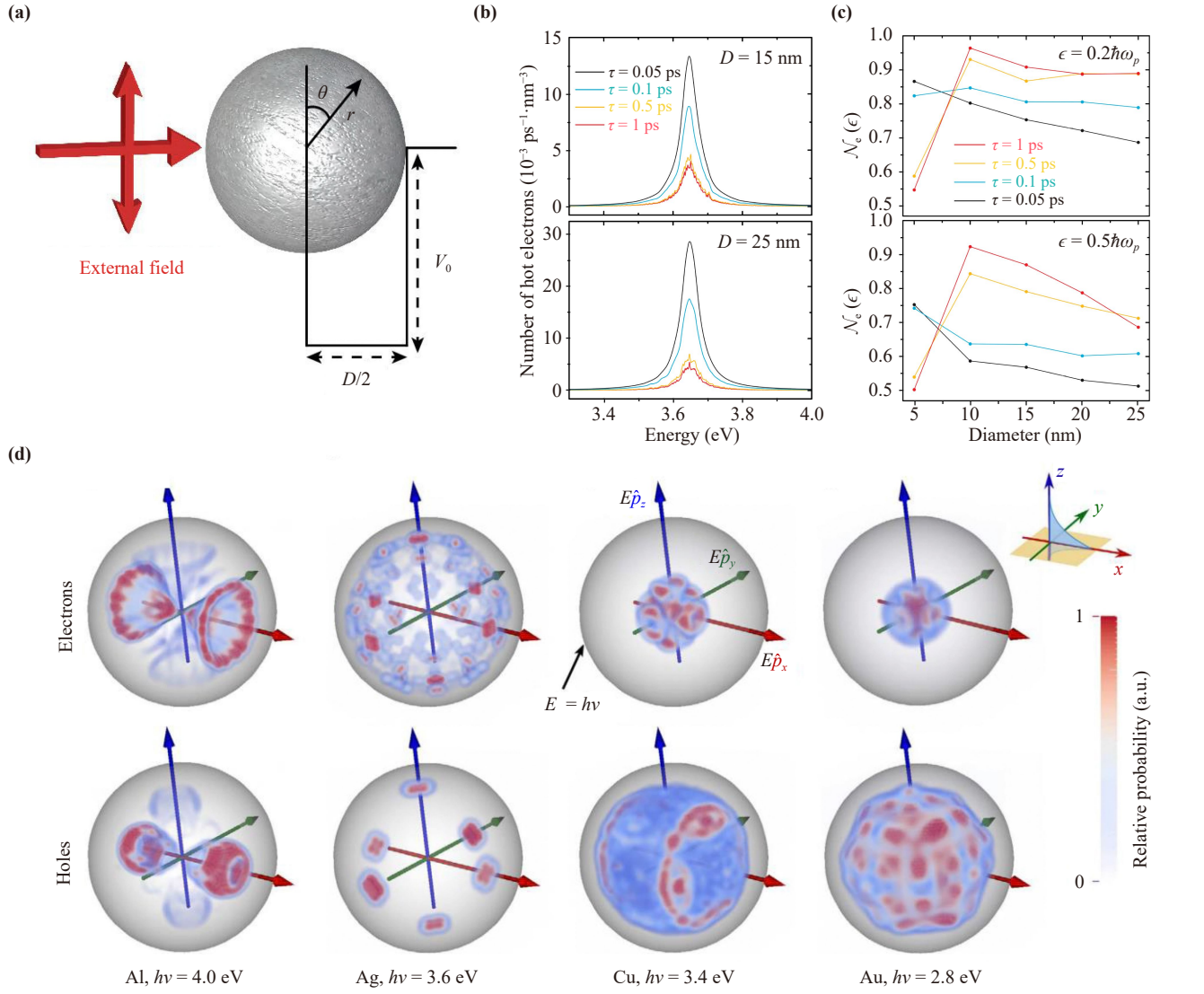

Fig. 9 **(a)** Plasmon-induced hot electron production in a silver nanoparticle of diameter D as a finite potential well of depth V_0 and radius to $D/2$. **(b)** Number of hot electrons generated per unit of time as a function of energy of incident photon for different carrier lifetime ranging from 0.05 to 1 ps. Top panel is the result for an Au NP $D = 15$ nm and bottom is for $D = 20$ nm. **(c)** FoM $\mathcal{N}_e(\varepsilon)$ as the function of particle size for different carrier lifetime raging from 0.05 to 1 ps. Top panel is the result for $\varepsilon = 0.2\ \hbar\omega_p$ and bottom for $\varepsilon = 0.5\ \hbar\omega_p$. **(d)** Hot-carrier energy and momentum-direction distribution in aluminum, silver, copper and gold spherical. Reproduced from Ref. [144].

results about relaxation times at the Γ, L, and X valleys were very consistent with ultrafast optical experiments data. Teranishi's group [148] used time-resolved IR (TR-IR) spectroscopy to observe the LSPR-induced hot carriers transfer process in CdS/CuS heterostructure, which provided a new insight of carriers transfer mechanism. The quantum yields and charge separations time of this plasmon-induced transit carrier transfer (PITCT) is 19% and 9.2 μs. Halas *et al.* [149] demonstrated the branching ratio between two decay mechanisms can be adjust by plasmonic resonance mode, which is influenced by the symmetry of system. They found the symmetry-broken system always show large LSPR sensitivity. Zhang *et al.* [150] built a theoretical framework for the hot-electron generation process based on a quantum-mechanical model. GW-like approximation is introduced to interpret the e–e scattering in following relaxation process. While there has been a great deal of theoretical work about mechanism of LSPR-enhanced PD, it is still necessary to combine these theories, which are effective in different ranges, to achieve a deeper understanding and predictability in plasmon-induced hot electron experiments.

The primary challenge encountered in the development of LSPR photodetectors lies in optimizing the interface between the plasmonic materials layer and photoresponse

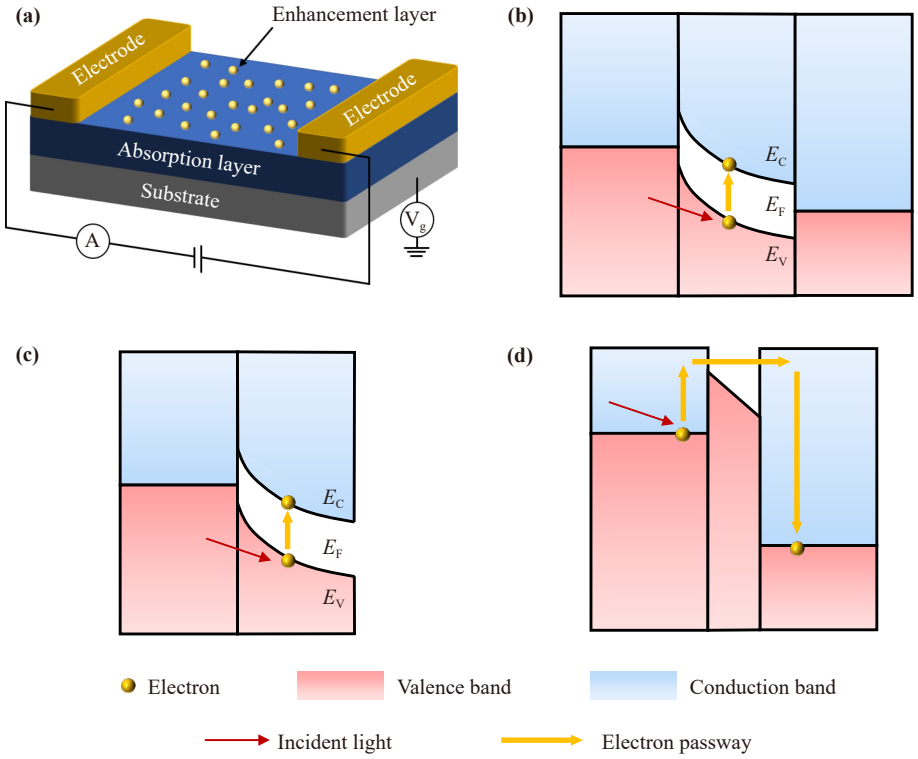

Fig. 10 **(a)** Scheme of localized surface plasmon resonance enhanced photodetector structure. Energy band diagrams of **(b)** metal–semiconductor–metal, **(c)** Schottky diode and **(d)** tunnel junction photodetectors.

layer. Near-field effects, mainly working at the nanoscale, require close contact between these components. However, direct contact might generate some problems, such as introducing new defects and causing nonradiative recombination. Semiconductor nanocrystals are often coated with long organic ligands on the surface for protection, however, these long organic ligands increase the gap between the plasmonic materials layer and photoresponse layer, reducing near-field effects and hindering hot-electron transfer. Therefore, ligands engineering and surface treatments are crucial for optimizing LSPR photodetector performance. Furthermore, selecting plasmonic materials with suitable bandgap can enhance carrier transfer efficiency. In summary, interface engineering constitutes a complex and integrated process and further studies are warranted to develop more effective interfaces.

5 High performance plasmonic photodetectors

After introducing the basic theory and properties of LSPR, this section focuses on its applications in photodetectors and other fields. We categorize the LSPR photodetectors based on the applied wavelength, ranging from ultraviolet to visible and infrared. As the wavelength varies, LSPR materials also change, transitioning from noble metals such as gold and silver to semiconductors like indium oxide and silicon. Finally, we briefly introduce LSPR applications in other fields such as biosensing, Raman spectroscopy enhancement, and photocatalysis.

5.1 Introduction of plasmonic photodetector

A general structure of LSPR photodetector is described in Fig. 10(a), where plasmonic layer are served as enhancement layer. Electron–hole pairs are generated through interband transition in the absorption layer, which can be enhanced by the plasmon-induced near-field. Meanwhile, plasmon-induced hot electrons in the LSPR layer are injected into the absorption layer to participate in the photocurrent through the Schottky barrier. Figure 10(b) is the metal–semiconductor–metal photodetector with plasmonic structures. To detect photons with an energy below the bandgap but larger than the work function of the junction, the current studied LSPR photodetector is mainly focused on the Schottky type [Fig. 10(c)]. The earliest plasmonic photodetector was based on metal–insulator–metal (MIM) structure Fig. 10(d), which has been studied for about 40 years [151]. Figures 10(b)–(d) illustrated the energy change of electrons after being excited by incident light.

First, we introduce some important figures of merit for photodetector: responsivity (R), noise-equivalent power (NEP), detectivity (D^*) and external quantum efficiency (EQE). The responsivity of a photodetector, which evaluates the performance of a detection system,

is defined as

$$R = \frac{I_{\text{ph}} - I_{\text{dark}}}{P}. \tag{22}$$

I_{ph} and I_{dark} represent the photocurrent and the dark current, respectively. P is the total laser intensity applied to the sample. Responsivity is the basic characteristic parameter of the photodetector. However, it cannot reflect the performance of the photodetector directly since it depends on the incident light power.

Noise-equivalent power (NEP) is the minimum detectable power, which is defined as the incident light power when the signal-to-noise ratio is one of a one Hertz output bandwidth, meaning that the photocurrent I_{p} is equal to the noise current I_{b}. NEP can be calculated by

$$\text{NEP} = \frac{I_{\text{b}}}{R \cdot \sqrt{\text{Hz}}}. \tag{23}$$

Specific detectivity (D^*) is the most important parameter for characterizing the performance of photodetector. From Eq. (23) we can see, the NEP depends on the photocurrent, which is influenced by the active optical are A_{opt}. Thus D^* is defined as

$$D^* = \frac{\sqrt{A}}{\text{NEP}}. \tag{24}$$

There are also some other parameters to reflect the photodetectors' performance. Response time (τ) is the time needed for the increase of output photocurrent from 10% to 90% in response to an incident optical signal. Quantum efficiency (QE), which includes both internal and external quantum efficiency, characterizes the photon coverage efficiency. Internal quantum efficiency (IQE) is the ratio of the number of photo-generated charge carriers collected by the electrode to the number of photons absorbed by the photodetector. External quantum efficiency (EQE) is the ratio of the number of photo-generated charge carriers collected by the electrode to the total number of incident photons. And they can be expressed as follows:

$$\text{EQE} = \frac{\text{Electrons/s}}{\text{Photons/s}} = \frac{P/(h\nu)}{I/e}, \tag{25}$$

$$\text{IQE} = \frac{\text{Electrons/s}}{\text{Absorbed photons/s}} = \frac{P/(h\nu)}{P_{\text{int}}/h}. \tag{26}$$

5.2 High performance plasmonic photodetectors

Based on the resonance frequency of plasmonic materials, LSPR effects can enhance the performance of PDs in UV to IR ranges. In this section, the recent progress of LSPR photodetectors covering UV, Vis and IR windows will be introduced.

5.2.1 UV LSPR photodetector

Ultraviolet (UV) photodetectors have been widely used in many applications such as space communications, flame sensors, and oil pollution monitoring. Due to its anti-interference of electromagnetic radiation and high-security at the wavelength below 400 nm. Wide bandgap semiconductors such as ZnO, indium–gallium–zinc oxide (IGZO), GaN and Ga_2O_3 [152] are widely used as absorbing layers in UV photodetectors. UV LSPR photodetectors, composing of plasmonic nanostructures and UV sensitive materials, bring unexpected enhancement of device performance.

ZnO-based semiconductors are regarded as one of the most ideal materials for UV photodetectors due to its intrinsic wide bandgap (3.7 eV at room temperature) and large exciton binding energy (60 meV). Great efforts have been made to focus on how to enhance the performance of ZnO-based UV photodetector via the LSPR effects of noble metals. In 2014, Gogurla *et al.* [44] achieved an 80-fold increase of photoresponse at 335 nm using Au-ZnO nanocomposite [Figs. 11(a, b)]. The increased responsivity was mainly caused by electron interband transition occurring in Au NPs and transferring to ZnO. LSPR effects can match different ZnO PDs with various structures, such as ZnO heterojunction photodetector, multilayer ZnO photodetector or low-dimensional ZnO structures photodetector. In 2017, Wang *et al.* [153] reported a wavelength selective Ag NPs/ZnO film photodetector fabricated via a magnetron sputtering technique [Fig. 11(c)]. The device exhibited a high wavelength selectivity with responsivity increasing only at 380 nm and decreasing significantly at other wavelengths compared to pristine ZnO film photodetector. This was attributed to the narrow-band quadrupole plasmon resonance of Ag NPs. Besides, the dark current decreased from 60 to 38 mA/cm^2, which may be due to the localized Schottky junction between ZnO film and Ag NPs. Ouyang [154] built a type-II heterojunction photodetector formed by $CdMoO_4$ microplates and ZnO film. They achieved a twice higher photocurrent and half decay time simultaneously. Liu *et al.* [155] developed ZnO/Au heterostructures with self-assembled Au nanoantennas. They demonstrated a novel approach to fabricate self-assembled Au nanoantennas with island-like morphology via solid-state dewetting and achieved a configuration-tunable LSPR with different size distributions and morphologies. As a result, the photocurrent increased obviously after being decorated with Au nanoantennas and the photoresponse could extend to the visible region due to the broad-band LSPR enhancement. In 2019, Li *et al.* [156] developed a ZnO/Ag/ZnO/Ag/ZnO multi-layer-structured UV photodetector, which displayed a better performance than single-layer device.

Compared to the film absorption layer, low-dimensional ZnO structures have a more effective light absorption ability in the axial direction. Liu's group [157]

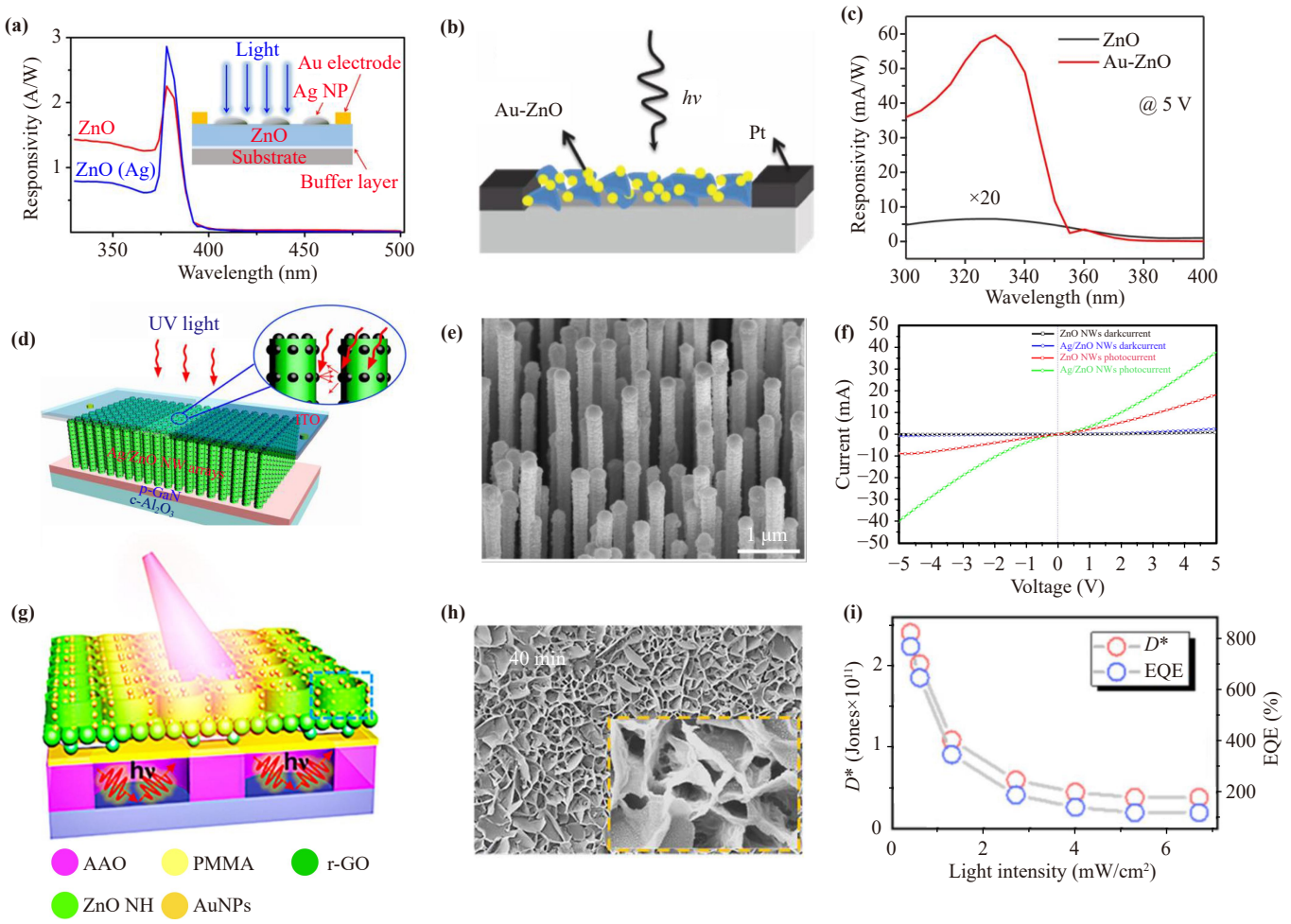

Fig. 11 **(a)** Responsivity spectrum of Ag-ZnO UV LSPR photodetector from 300 to 500 nm and structure. The buffer layer is ZnO and the substrate is sapphire. **(b)** Schematic of Au-ZnO UV LSPR photodetector with Pt electrode. **(c)** Responsivity spectrum of ZnO and Au-ZnO devices from 300 to 400 nm at 5 V. **(d)** Schematic of Ag NPs/ZnO nanowires (NW) @GaN UV photodetector. **(e)** High-magnification SEM image of 10 nm Ag NPs coated on ZnO NW arrays. **(f)** Darkcurrent and photocurrent as a function of applied voltage for pure ZnO and Ag-ZnO device. **(g)** Schematic of Au@ZnO nanoholes(HN) photodetector. **(h)** SEM images of the morphologies of the Au NP/ZnO HN for 40 min growth. **(i)** Detectivity and EQE of ZnO HN photodetector fabricated with a growth duration of 40 min as a function of light intensity. (a) Reproduced from Ref. [153]. (d–f) Reproduced from Ref. [157]. (b, c) Reproduced from Ref. [44]. (g–i) Reproduced from Ref. [162].

constructed a composite of Ag NPs@ZnO nanowire (NW) arrays on a GaN thin film which was fabricated via chemical vapor deposition (CVD) and thermal evaporation [Figs. 11(d, e)]. This device exhibited double photocurrent and fourfold accelerated photoresponse time due to the multiple scattering of elongated optical path length and absorption volumes by vertically aligned nanowires [Fig. 11(f)]. Lu *et al.* [158] fabricated Al NPs/ZnO NRs hybrid structure and obtained 12 times higher of responsivity. Yang *et al.* [159] decorated ZnO nanorods (NRs) by Ag NPs via a hydrothermal method, achieving a 47-fold enhancement in specific detectivity compared to pristine ZnO. Hsu *et al.* [160] fabricated a Pb@NiO/ZnO p–n heterojunction nanowires UV-Vis photodetector, which Pb NPs offered a strong localized electrical field for significant light absorption. They measured the photoelectrical properties from UV to green light region and the I_{green}/I_{dark}, I_{blue}/I_{dark}, and I_{UV}/I_{dark} ratios of the photodetector were 91.4, 403.2, and 1.25×10^5, respectively. Later, Noh's group [161] achieved a higher performance with the similar structure by positioning Ag NPs using intense pulsed light (IPL) irradiation in silver nitrate ($AgNO_3$) aqueous solution. Except for nanowires. Li *et al.* [162] designed an Au NPs self-assembled ZnO honeycomb nano-mesh (Au NP/ZnO HN) photodetector [Figs. 10(g, h)]. A remarkable enhancement of light absorption was achieved during the cyclic light between anodic aluminum oxide matrixes and Au NPs. They gained the highest detectivity about 6.13×10^{11} Jones and 774% EQE in this device by optimizing the growth duration time, pore diameter and geometric effect [Fig. 11(i)]. Li *et al.* [163] designed a self-power photodetector utilizing ZnO/CuO core–shell nanorods decorated by Au NPs, which exhibited the coupling of piezo-

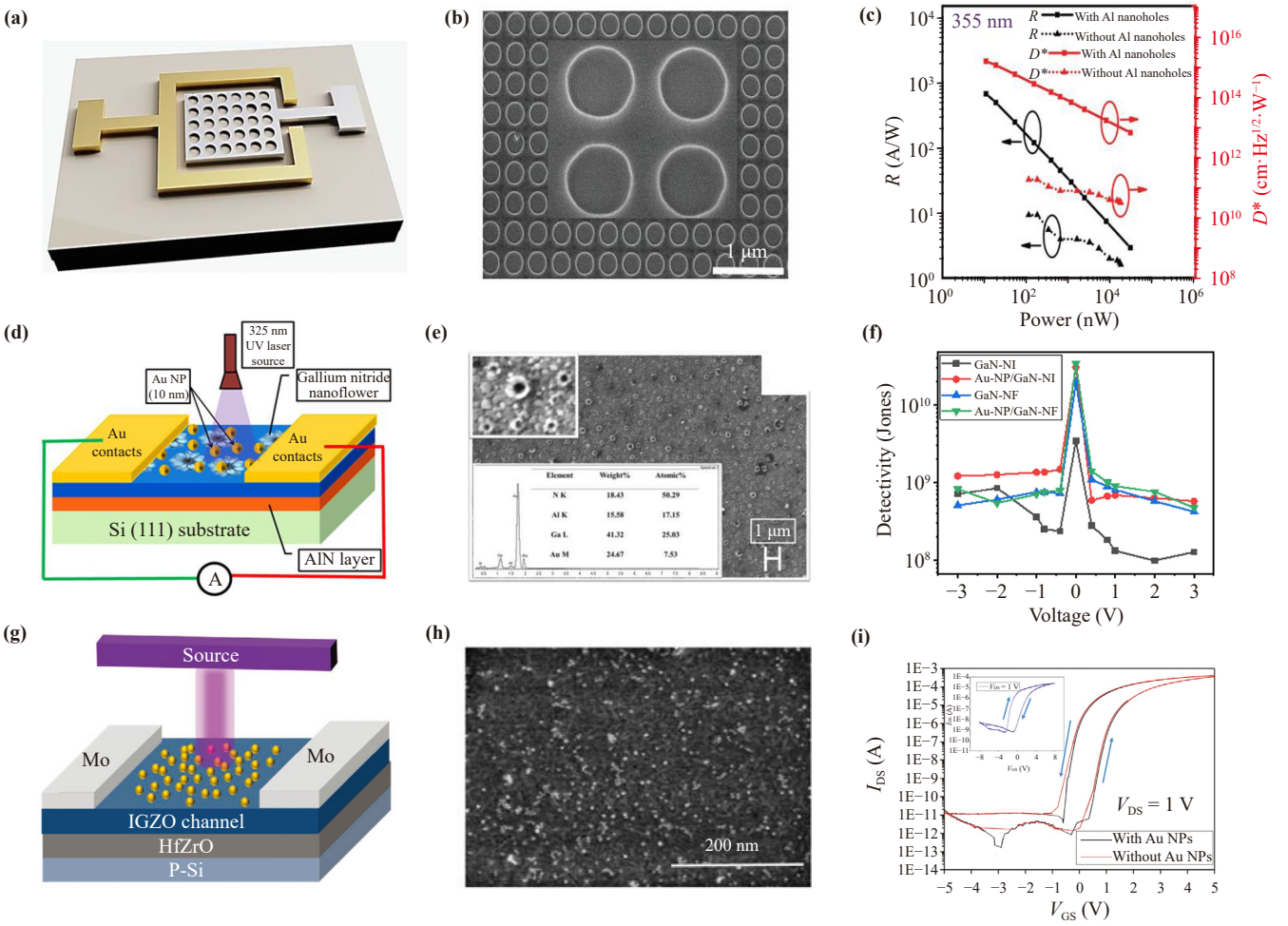

Fig. 12 **(a)** Schematic of Al nanoholes GaN UV photodetector. **(b)** SEM of the periodic Al Nanoholes array with 220 nm diameter and 320 nm periodicity. **(c)** Responsivity and detectivity as the functions of illumination power under 355 nm. **(d)** Schematic of Au NP@GaN-nanoflowers (NF) photodetector. **(e)** Field emission scanning electron microscopy (FESEM) image of Au-NP@GaN-NFs, inset shows its higher magnification image. **(f)** Detectivity as a function of bias voltages of four kinds of photodetector device. **(g)** Schematic of the Au NPs/IGZO hybrid ferroelectric photodetector. **(h)** High resolution SEM image of the hybrid photodetector. The white bright spot are Au NPs and mean size is ~ 5 nm. **(i)** The transfer curves of the ferroelectric phototransistor at room temperature, both with (black line) and without (red line) Au NPs. The inset displays the transfer characteristic of the HfO_2 gate. (a–c) Reproduced from Ref. [79]. (d–f) Reproduced from Ref. [164]. (g–i) Reproduced from Ref. [168].

phototronic, pyro-phototronic and LSPR effects simultaneously. The responsivity and detectivity was enhanced by 17× and 12× after being decorated with Au NPs.

Noble metal plasmonic structures are also effective in other materials-based UV PDs, such as GaN, Ga_2O_3 and other wide-bandgap semiconductors. Dubey's group [79] designed a periodic aluminum nanohole array on GaN substrate and got a highest detectivity of 1.48×10^{15} Jones among GaN-based PDs at that time [Figs. 12(a)–(c)]. Goswami *et al.* [164] reported an Au NPs/GaN self-power photodetector by covering the GaN nanostructures (nanoislands and nanoflowers) with Au NPs, which were grown via plasma-assisted molecular beam epitaxy technique [Figs. 12(d, e)]. Adequate contact between GaN and Au NPs increased the transfer of hot electrons generated by Au NPs into GaN layer, resulting in high responsivity (380 mA/W), detectivity (3.38×10^{10} Jones) and EQE (145.5%) [Fig. 11(f)]. Kunwar *et al.* [165] deposited monometallic Au, Ag NPs and bimetallic alloy AgAu NPs on GaN UV PD via solid-state dewetting approach. They gained a detectivity of 2.4×10^{12} Jones and EQE of 3.6×10^4 % at 385 nm in Ag_4Au_3/GaN device. Later, Lin *et al.* [166] used tri-metallic AgAuCu NPs to enhance GaN UV PD. According to FDTD simulation, they demonstrated that AgAuCu NPs had a much stronger near-field enhancement and they achieved the highest detectivity of 3.2×10^{12} Jones. Arora *et al.* [167] deposited Ag NPs onto the β-Ga_2O_3 to create an Ag NPs@ Ga_2O_3 thin film and they first observed a clear photoresponse in both UV-A band (320–400 nm)

and UV-C band (10–280 nm). Liu *et al.* [168] used Au NPs and hafnium zirconium oxide (HfZrO) film to improve the IGZO photodetector performance page-break-before:always[Figs. 12(g, h)]. They obtained a high responsivity (714.6 A/W) and detectivity (5.4×10^{12} Jones) and a low dark current (1.1×10^{-12} A) due to the combined effects of strong ferroelectric-localized field induced by HfZrO film and increased light absorption by Au NPs [Fig. 12(i)]. Han's group [169] covered 20–40 nm Ag NPs on solar blind MgZnO PD, resulting in a 226-fold increase of photoresponse at 235 nm. Shi *et al.* [170] assembled Al crescent arrays on boron-doped diamond thin films using a nanosphere lithography strategy. The optical responsivity of the device was an order of magnitude higher across the 200–600 nm range compared to bare diamond detectors, attributing to the improved optical absorption in the semiconductor layer due to near-field optical coupling between Al LSPRs and diamond. Mondal *et al.* [171] utilized Al NPs to modify erbium-doped titanium dioxide (Er:TiO_2) thin films for ultraviolet photodetectors. The photocurrent-to-dark current ratio increased by approximately 3.5 times after the incorporation of Al NPs. The responsivity of approximately 8000 A/W at 375 nm, which was approximately 2300 times higher compared to the bare Er:TiO_2 device with responsivity of 3.5 A/W. The detectivity reached 1.13×10^{12} Jones at 330 nm.

5.2.2 Visible LSPR photodetector

Visible photodetectors, which detect light in the range of 400 to 700 nm, are commonly used in a variety of applications, including digital cameras and optical communication. The recently studied visible photodetectors are almost based on two-dimensional semiconductors, such as graphene and transition metal dichalcogenides (TMDs). Plasmonic structures can also be used to induce LSPR fields and enhance the performance of these visible photodetectors.

Graphene is a promising two-dimensional material for visible PD because of its unique properties such as high carrier density, exceptional electron mobility (100 000 $cm^2 \cdot V^{-1} \cdot s^{-1}$), mechanical flexibility and broad spectral bandwidth. However, the relatively low light absorption ability for single-sheet graphene in visible region and ultrashort carrier lifetime greatly restrict its further applications. To overcome these limitations, plasmonic metal nanostructures are always employed to enhance light absorption. Fang *et al.* [172] designed a graphene-Au antennas-graphene sandwich structure to enhance the performance of photodetector [Figs. 13(a, b)]. Plasmon-induced antenna near field assisted the graphene-based photodetector in achieving IQE from 2.3% to 20% in visible and near-infrared regions. Hot electrons excited in Au antennas could transfer directly into the conduction band of graphene, leading to a lossless increase of photocurrent and obtaining an 800% enhancement in photocurrent. They also demonstrated that the Au heptamer antenna brought higher photocurrent without angle dependence, while the Au dimer array exhibited the reverse result [Fig. 13(c)]. Lee *et al.* [173] developed a self-reduction method to control the Au NPs density on the monolayer graphene based on the reduction potential difference between graphene and Au^{3+} precursor. They observed a red-shift in LSPR peak from 560 to 620 nm with increasing the Au NPs density. Jang *et al.* [174] proposed a pentacene-graphene-Au NPs hybrid structure multifunction photodetector to detect and store photonic signals simultaneously [Figs. 12(d)–(f)]. Au NPs were inserted between the blocking and tunneling dielectric and served as both a plasmonic structure and a charge-trapping layer to store the photonic signals. This device exhibited a broadband photoresponse between 400 to 800 nm, remarkable responsivity of 700 A/W under 0.1 V bias and highest detectivity is 10^{13} Jones at 520 nm.

MoS_2 possesses a direct bandgap (1.8 eV) and high absorption coefficient, which render it potential for visible light detection. Miao *et al.* [175] demonstrated that a three-fold increase of photocurrent in periodic Au NPs nanoarrays on MoS_2 phototransistors due to the plasmon resonance caused by the near-field oscillation and scattering effect of the periodic Au nanoarrays. Based on this theory, Li *et al.* [81] constructed a periodic Au grating/monolayer MoS_2 structure by placing two different sizes of Au NPs on MoS_2 layer [Figs. 14(a, b)]. The intensity and wavelength of the LSPR peak can be controlled by the grating period. The photocurrent increased 111 times using mixed two sizes of Au NPs grating, which was much higher than that for only single size Au NPs, i.e., 3.7 times for NP I and 1.9 times for NP II [Fig. 14(c)]. Selamneni *et al.* [176] compared the effects of three metal NPs (Au, Pt and Pd) on MoS_2 visible PDs. Au NP-MoS_2 system showed the highest responsivity of 99.3 and 46.03 mA/W under visible and near-infrared light, respectively. Later, Li *et al.* [177] proposed an Au–MoS_2–Au structure photodetector with sandwiching a MoS_2 flake between double-layer Au NPs [Fig. 14(d)]. They simulated the electric field distribution near the Au NPs and observed a significant increase of field intensity in the gap between two Au NPs layers occupied by MoS_2 layer [Fig. 14(e)]. A high performance of this Au–MoS_2–Au structure was obtained due to the better light absorption [Fig. 14(f)]. Except for sheet structure, Dravid's group [178] designed a Au/MoS_2 core-shell structure plasmonic photodetector with Au core encapsulated by multilayer MoS_2 shells [Figs. 14(g, h)]. The photocurrent measured under 50 μW illumination was ~29 and ~3 μA for the device with and without Au/MoS_2 core–shell NPs, respectively [Fig. 14(i)]. Additionally, the photoresponsivity of 11.2 A/W was two orders of magnitude higher than that for only monolayer MoS_2 photodetectors. Furthermore, Zhang *et al.* [179] proposed an approach to enhance the performance of a

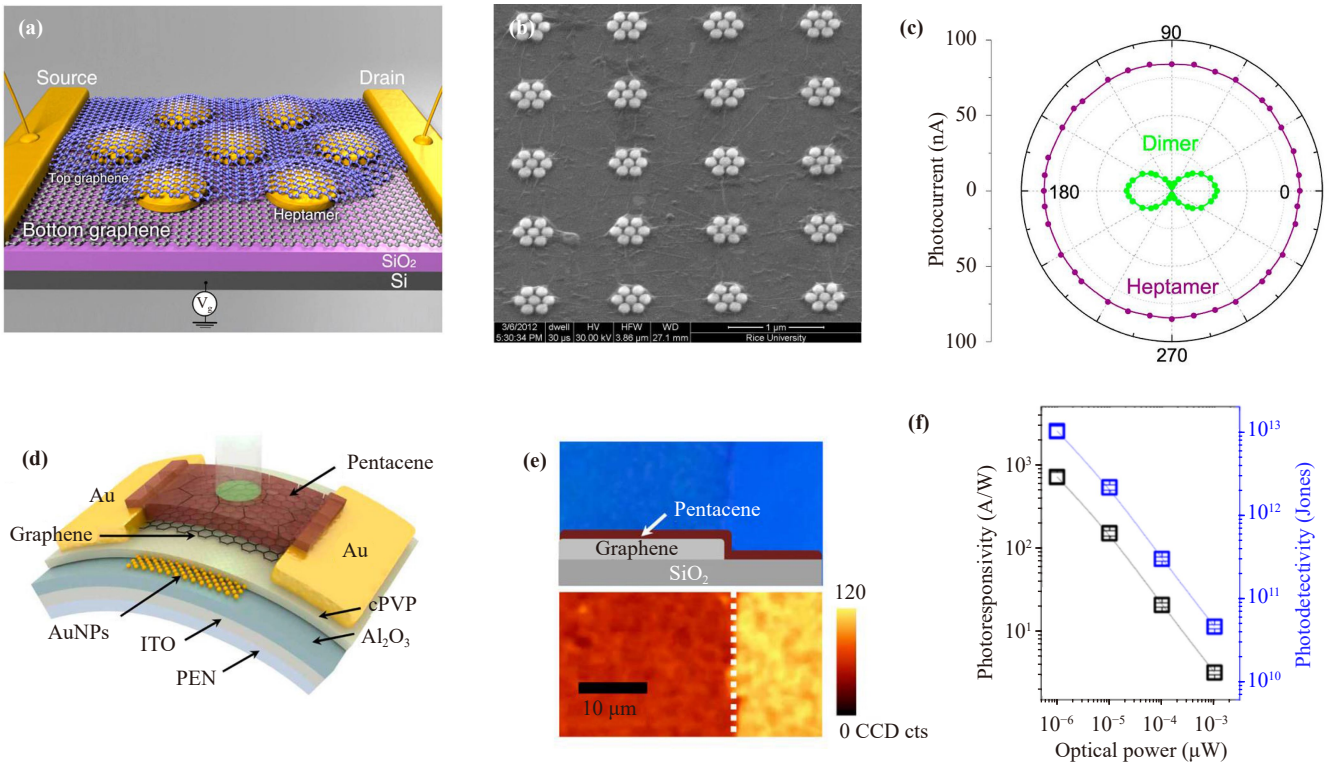

Fig. 13 **(a)** Schematic of gold antenna@graphene boardband photodetector. **(b)** SEM image of Au heptamer array. **(c)** Photocurrent polarization dependence for dimer antennas (green dots) and heptamer antennas (purple dots). **(d)** Schematic of pentacene/Au NPs/graphene photodetector. **(e)** Optical microscopy image (upper panel) and integrated PL intensity map (lower panel) of the pentacene films deposited on the SiO_2 substrate and graphene. **(f)** Photoresponsivity and photodetectivity under a fix illumination wavelength of 520 nm as a function of optical power. (a–c) Reproduced from Ref. [172]. (d–f) Reproduced from Ref. [174].

MoS_2/ZnO heterostructure in both UV and visible regions simultaneously by modifying Au NPs. The responsivity, external quantum efficiency and detectivity of this device were enhanced by 9 times, 9 times and 15 times, respectively, due to the LSPR effects of Au NPs.

5.2.3 IR LSPR photodetector

Infrared photodetectors detecting electromagnetic waves above 700 nm play an important role in night vision, communication, military detecting and bio-imaging, etc. Compared to UV-Vis LSPR photodetectors, the development on LSPR in IR region is much lag far behind. This mainly caused by two reasons: (i) Wavelength mismatch between LSPR peak of commonly-used metallic plasmonic structures and infrared region, especially for MWIR (3–5 μm) and LWIR (8–14 μm) ranges. (ii) Undeveloped plasmonic materials or structures with LSPR in IR region. The current study on IR LSPR PDs are mainly based on noble metal structures and some kinds of semiconductors with low carrier concentrations [180].

Fang *et al.* [181] utilized graphene nanodisk arrays to achieve tunable IR absorption enhancement based on graphene's spontaneous surface plasmon resonance [Figs. 15(a)–(c)]. The LSPR frequency $\omega_p \sim (E_F/D)^{1/2}$ could be modified by tuning the Fermi energy E_F via applying a voltage, and the diameter of graphene nanodisks (D). Both transmittance, absorbance and reflectance peak red-shifted with the nanodisk diameter decreasing and blue-shifted with gap decreasing. Their single layer graphene nanodisks displayed more than 30% optical absorption, which is much higher than 2.3% for single undoped graphene layer. Xia *et al.* [182] reported an Au NRs/graphene heterojunction NIR photodetector. The Au NRs with 17 nm diameter and 120 nm length exhibited LSPR peak around 1250 nm, which helped to obtain a photogain (G) of 10^9 at 1310 nm. Deng and his co-workers [183] deposited two modes of graphene plasmonic ribbons, with widths of 80 and 160 nm, respectively. The hybrid array exhibited an extremely wide extinction spectrum. Chen *et al.* [82] fabricated Au NPs array by nanosphere lithography approach on graphene to introduce a light-trapping effect [Figs. 15(d)–(f)]. Due to the LSPR effect induced by Au NPs array and built-in field effect by the contact between graphene and silicon, they obtained a record responsivity of 83 A/W at 1.55 μm [Fig. 15(f)]. Rohizat's group [184] decorated the reduced graphene oxide (rGO) with Au

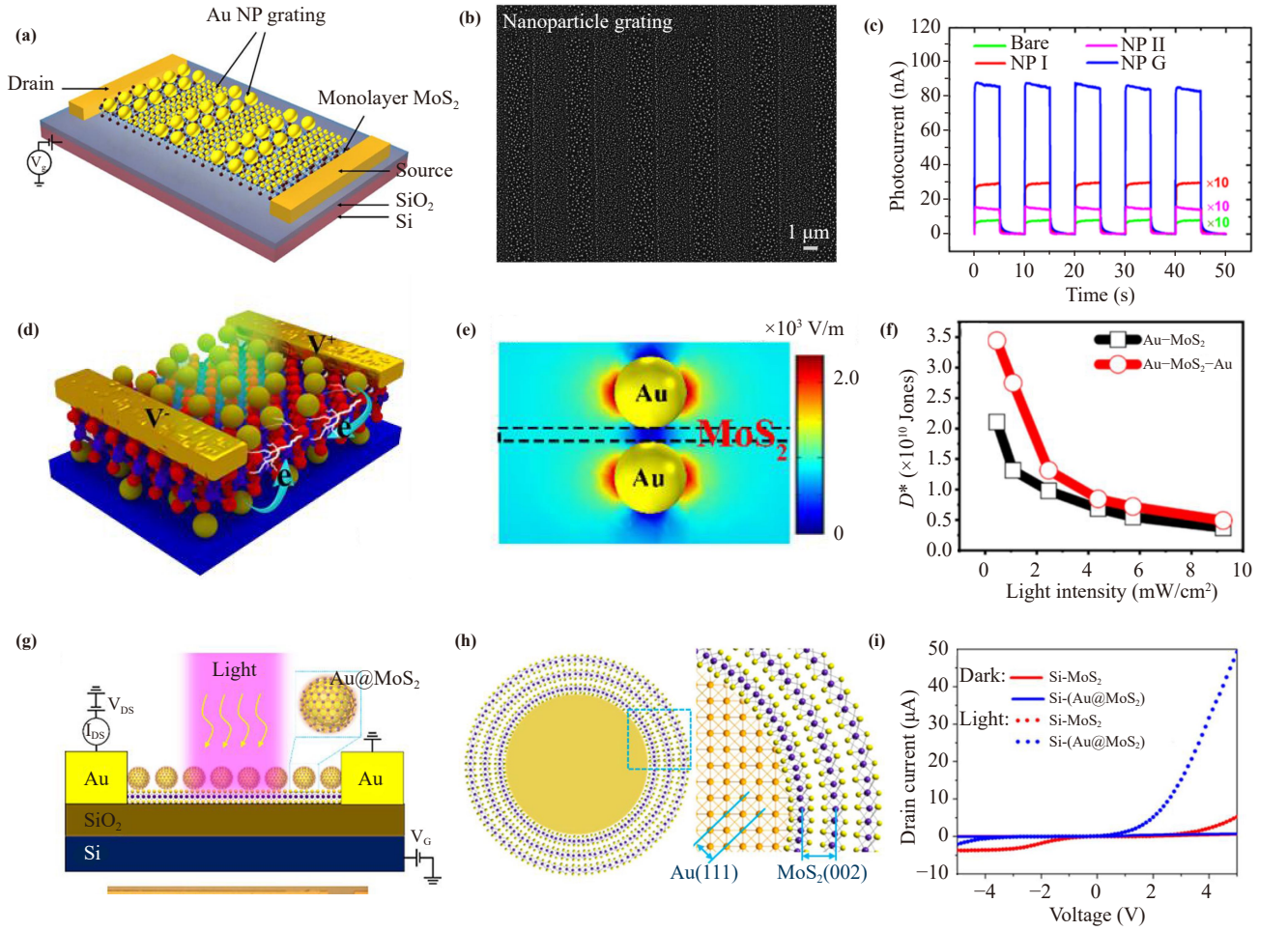

Fig. 14 **(a)** Schematic of Au NP grating/monolayer MoS_2 hybrid photodetector. **(b)** SEM image of Au NP grating structure. The period is 4 μm and the duty ratio is 1:1. The diameter of larger nanoparticle is 10 nm, and the smaller one is 5 nm. **(c)** Photocurrent cycle of bare MoS_2 PD, MoS_2 with different size Au NPs, and MoS_2 with Au gating photodetector. NP I: 5 nm. NP II: 10 nm. **(d)** Schematic of Au–MoS_2–Au photodetector. **(e)** Electrical field distribution of Au–MoS_2–Au structure through COMSOL simulation. **(f)** Specific detectivity of Au–MoS_2 and Au–MoS_2–Au devices as a function of light intensity upon 3V bias and 532 nm illumination. **(g)** Schematic of Au@MoS_2 field-effect phototransistors. **(h)** Concept and structure of the Au@MoS_2 core-shell structure. **(i)** Drain current as a function of bias voltage under 50 μW white light illumination. (a–c) Reproduced from Ref. [81]. (d–f) Reproduced from Ref. [177]. (g–i) Reproduced from Ref. [178].

NPs and Ag NPs, achieving excellent performance of IR PDs at 680 nm. Apart from this, Dai *et al.* [185] coupled layer graphene onto copper substrates via chemical vapor deposition, achieving near-field infrared nanoimaging of graphene.

Plasmonic semiconductor materials with LSPR peak in IR region, such as doped silicon, doped metal oxide ($Sn:In_2O_3$), TiN and non-stoichiometric metal chalcogenides (MoS_x), have recently received widespread attentions due to their tunable charge carrier types and densities. Although extensive efforts have been made on synthetic control of semiconductor plasmonic materials and tune of LSPR properties, the study of these semiconductor plasmonic structures on IR photodetectors are in the early stage. In 2016, Lu *et al.* [102] reported the first work about semiconductor plasmonic nanoparticles enhancing photodetector. They used ITO NPs with LSPR peak in NIR region to enhance the single-layer graphene (SLG)/germanium nanoneedles (Ge NNs) array NIR PD [Figs. 16(a, b)]. With the presence of ITO NPs, the photocurrent and on/off ratio increased by 144% and 166%, separately [Fig. 16(c)]. The highest detectivity was 2.28×10^{13} Jones at 1550 nm. They demonstrated that the well performance of their device was attributed to the light confinement of Ge NNs arrays and hot electron injection from plasmonic ITO NPs via finite-element method (FEM) simulation. Podder *et al.* [186] reported that titanium nitride (TiN) NPs possess plasmonic properties, especially in high temperature. Thus, they fabricated a TiN-based visible-NIR photodetector [Figs. 16(d, e)]. TiN NPs were synthesized by reactive magnetron sputtering and they observed TiN as well as TiNO phase were presented in the resulting sample, which exhibited plasmon absorption band in visible and NIR separately.

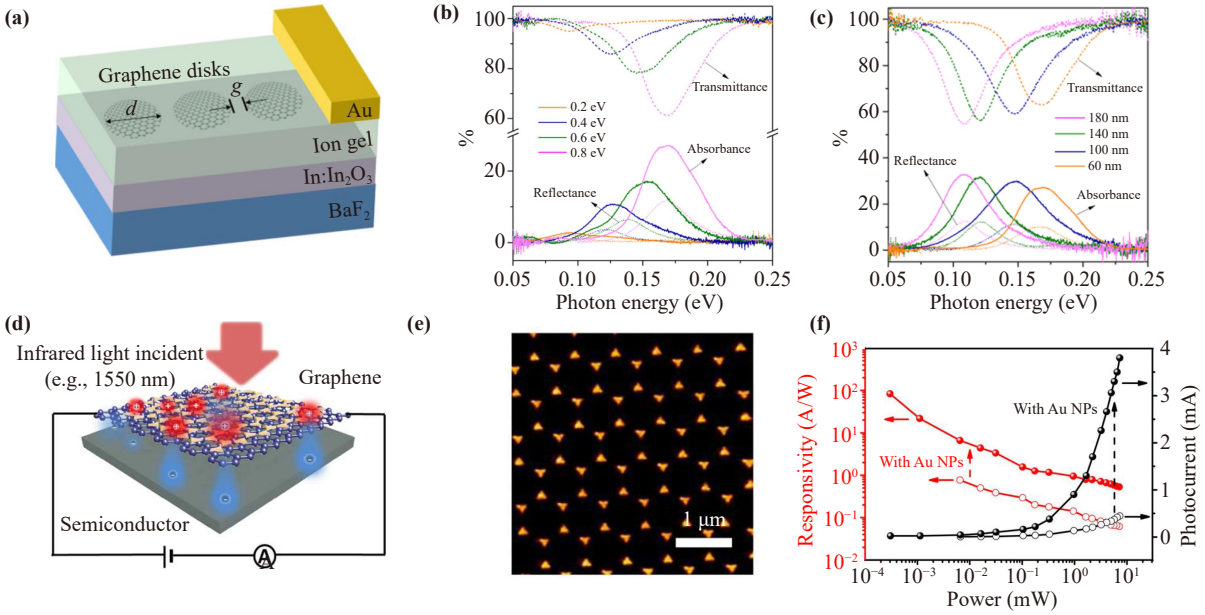

Fig. 15 **(a)** Schematic of graphene SWIR photodetector. **(b)** SEM image of Au NP array on graphene. **(c)** Photoresponse and photocurrent of device with and without Au NPs versus illumination power at a wavelength of 1550 nm. **(d)** Schematic of graphene nanodisk arrays. The graphene nanodisk arrays with 60 nm diameter and 30nm edge-to-edge gap was sandwiched between In-In_2O_3/BaF_2 substrate and ion-gel layer. Ion-gel layer with high-capacitance was used to tune the Fermi level of graphene nanodisks. **(e)** FTIR measurement results of transmittance, reflectance, and absorbance under different Fermi energy (0.2–0.8 eV). **(f)** FTIR measurement results of transmittance, reflectance, and absorbance under different disk diameter (60–180 nm). (a–c) Reproduced from Ref. [181]. (d–f) Reproduced from Ref. [82].

The IQE of the TiN-based device at 450 nm and 950 nm were 48% and 35%, the highest specific detectivity was 9×10^9 Jones at 950 nm [Fig. 16(f)]. To enhance the performance of IR PDs with longer detection wavelength, Ni *et al.* [103] utilized B-doped Si colloidal quantum dots with LSPR effects in MIR region to enhance the MIR photodetection of graphene [Fig. 16(g)]. The average diameter of B-doped Si QDs was 6 nm and the electric field distribution at Si QDs was calculated by FDTD [Fig. 16(h)]. The device showed the value of D^* about ~10^6 Jones in MIR region at 77 K, and D^* could be on the order of ~10^{13} Jones in UV-to-NIR region at room temperature [Fig. 16(i)].

5.3 Other applications based on LSPR photodetectors

5.3.1 LSPR bio-sensors

LSPR has attracted extensive attention in the field of biochemical sensing in recent years, it can be performed by detecting changes in the relevant frequency of the surface plasmon resonance in the presence of the target analyte, such as SPR biosensors [187] and LSPR biosensors [188–192]. Initially, LSPR biosensors faced challenges such as minimal resonance peak shifts, inadequate resonance intensity, broad linewidths and low peak-to-valley ratios [193, 194]. These limitations hindered their effiency in high-precision biochemical sensing. Great efforts have been made to raise the sensitive and precision of LSPR biosensors, such as changing LSPR nanoparticle shape, designing uniform array structure [195], combining with metamaterials [196], utilizing Fano effect [197] or using plasmonic metasurface [198]. Park *et al.* [199] developed nanoscale self-assembly star-shaped Au nanoparticles to improve the plasmonic sensitivity, which achieved 460-fold higher field density via plasmon coupling and 250–500 nm/RIU sensitivity. Wu *et al.* [197] designed a LSPR biosensor based on Fano resonance to break the limitations of traditional detection. Plasmonic metasurface is another potential way to enhance the sensitivity for biosensing. Zhu *et al.* [198] presented a low-cost bio-functionalized plasmonic metasurfaces with periodic gold nanobumps on a flexible light-weight polycarbonate substrate for highly sensitive label-free detection of tumor marker in human serum samples. The sensitivity reaches 454.4 nm/RIU. These high performance LSPR biosensors would inevitably promote the development and progress of medical care, food inspection and other fields.

5.3.2 LSPR photocatalysis

The photocatalytic reactions driven by LSPR have attracted increasing research interests because the hot carriers generated by LSPR decay possess higher energy compared to electrons generated in traditional photocatalysis. Plasmonic-metal-based photocatalysts can effi-

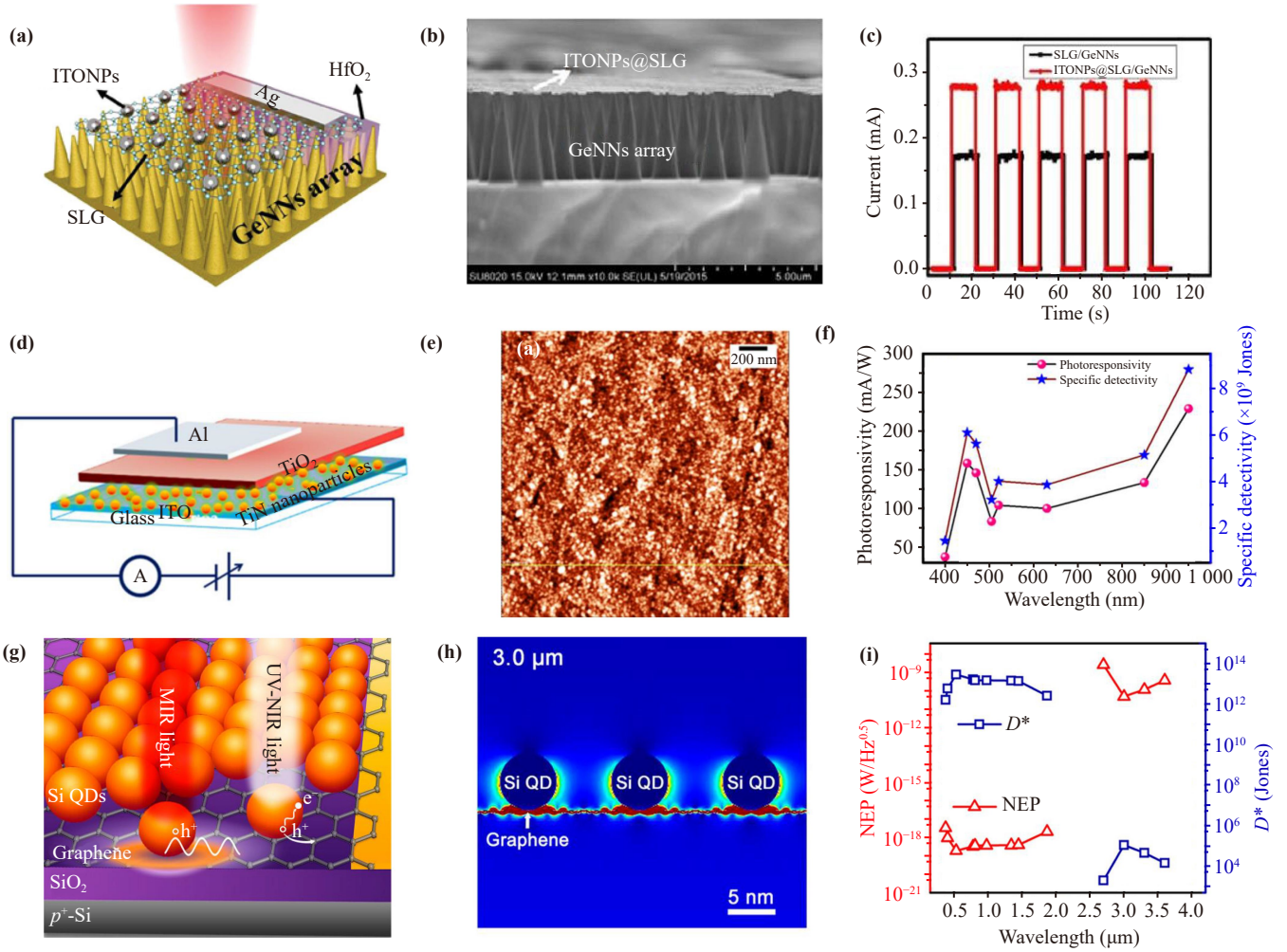

Fig. 16 **(a)** Schematic of ITONPs@SLG/GeNNs array NIRPD. **(b)** SEM image of ITONPs@SLG/GeNNs array NIRPD. The length of GeNN arrays is about 3 μm. **(c)** Photoresponse for devices with and without ITONPs modification under 1550 nm light illumination at V_{bias} = 0 V. **(d)** Schematic illustration of TiN-based visible-NIR photodetector. **(e)** AFM image of TiN surface morphology. **(f)** Photoresponsivity and specific detectivity of the device. **(g)** Structure of a Si-QD/graphene hybrid phototransistor. **(h)** Distribution of electric field ($|E|^2$) around B-doped Si QDs under 3.0 μm illumination. **(i)** NEP and specific detectivity of the device from 0.5 to 4 μm. The UV-to-NIR and MIR measurements were conducted at room temperature and 77 K, respectively. (a–c) Reproduced from Ref. [102]. (d–f) Reproduced from Ref. [186]. (g–i) Reproduced from Ref. [103].

ciently integrate light absorption, electric field, energetic carriers and thermal effects into one material, enabling the excitation and activation of inert molecules under mild reaction conditions.

Yamashita *et al.* [200] utilized MoO_{3-x} nanoplates to achieve LSPR in the visible to near-infrared region, enhancing hydrogen generation from ammonia borane decomposition. Dong *et al.* [201] utilized plasmonic $W_{18}O_{49}$ nanograsses to drive photocatalytic water reduction for hydrogen generation. Excited hot electrons were transferred from $W_{18}O_{49}$ to the conduction band of adjacent g-C_3N_4 nanosheets, facilitating proton reduction to hydrogen. The oxygen vacancies in plasmonic WO_{3-x} are easily removed in aqueous solutions, leading to a decrease in the LSPR intensity during photocatalytic hydrogen generation from water. Therefore, Lou *et al.* [202] proposed the concept of electron injection to maintain the stability of free carrier concentration in WO_{3-x} by creating a plasmonic heterostructure with CdS/WO_{3-x} nanowires. In this structure, photogenerated electrons in CdS were transfer to the conduction band of WO_{3-x}, thereby stabilizing the concentration of free carriers and enabling prolonged photocatalytic reactions.

5.3.3 LSPR enhanced Raman spectroscopy

Classical Raman spectroscopy are related to molecules with very low Raman efficiency, low concentration and quantities of sample. However, molecules located near structured metallic nanostructures, when excited by visible light, can exhibit a significant enhancement in Raman

scattering intensity, potentially reaching up to 10^{10}-fold, which is called surface enhanced Raman spectroscopy (SERS). SERS is an important molecular identification analytical tool based on vibrational fingerprints.

Mikac *et al.* [203] used 40 nm Ag nanoparticles to test Raman enhancement based on pyridine. The highest SERS enhancement factors for pyridine reached to 10^6. Chen *et al.* [204] demonstrated that Ag nanoparticle films regulated by alkane thiolate ligands enabled precise quantitative SERS measurements at the single-molecule level. Zhou *et al.* [205] developed Au/Ag core/shell nanoparticles embedded with 4-aminothiophenol as an internal reference, enabling quantitative measurement of analyte SERS signals. This strategy addressed the historical limitation of SERS primarily being employed for qualitative rather than quantitative analysis.

6 Conclusion and outlook

Compared to the conventional photodetector, plasmonic photodetectors exhibit high sensitivity, fast response times, and tunable photodetection range due to the capacity of plasmonic nanomaterials in light absorption enhancement and plasmon-induced hot electron injection. In this review, we first give a clear description of basic physical model of surface plasmons, then we introduce the tunability of LSPR frequency of plasmonic materials and enhancement mechanism for LSPR photodetector. At last, we highlight the recent developments on LSPR photodetectors based on the photodetection wavelength window. Although significant progress has been made in the design and fabrication of LSPR photodetectors, there are still some challenges and research directions needing further study.

(i) Infrared plasmonic materials and related photodetectors. The current most-used plasmonic materials focus on noble metals, especially gold and silver. In recent years, other low-dimensional plasmonic materials are explored to modulate LSPR frequency in recent years. However, their LSPR frequency mainly located at visible to near-infrared wavelength range. There are great demands in mid-infrared or longer infrared wavelength region, which has been the forefront of the current study of plasmonic materials and their related applications. While the integrating of plasmonic materials with the device on infrared wavelength using traditional physical methods cannot meet the requirements. Besides, the high cost and complex process also limit their further applications. To fulfill the full potential of plasmonic nanomaterials, an easy-handled and high-reproducible synthetic strategy for colloidal nanocrystals with LSPR frequency over a wide spectral window, especially in infrared wavelength region, is of critical importance. Combining morphology and size control with carrier density tuning for semiconductor plasmonic materials represents an efficient approach. Since the abundant synthetic chemistry of semiconductor nanocrystals, there are various carrier density tuning methods for semiconductor materials, such as doping and post-synthesis methods. These strategies are also applicable to different types of materials. Besides, the excellent solution-processability of these plasmonic semiconductor nanocrystals can render them integrating with photoelectric devices through low-cost and easy-handling spin-coating or drop-casting methods.

(ii) Interface between plasmonic materials and photoresponse layer. The obviously enhancement of photodetector performance by directly coating plasmonic materials onto photoresponse layer is attributed to the efficient charge transfer between plasmonic materials and photoresponse layer. However, the direct contact between the commonly used plasmonic metals with photoresponse layer can cause new defects, which may induce new recombination sites and trap the hot-carriers excited in the photoresponse layer, thus decreasing the amounts of photogenerated carriers. Besides, the energy transfer between the plasmonic materials and the neighboring photoresponse layer could also cause a loss of photogenerated carriers in the photoresponse layer, which will weaken the plasmonic enhancement. Furthermore, thermionic emission may be caused by the direct contact between the plasmonic materials and photoresponse layer, which could result in undesirable dark current, thus decreasing the photodetector performance. So rational interface engineering between plasmonic materials and photoresponse layer is needed minimize the problems discussed above. Therefore, surface engineering is required to modify the interface, reduce defects generated during material contact, and achieve efficient charge carrier transfer by selecting plasmonic materials with suitable bandgap, ligands exchange and surface post-treatments. In addition, device performance can also be enhanced through the design of novel LSPR structures, such as, integrating the plasmonic layer with the light-response layer or utilizing electromagnetic field simulations to determine the optimal distribution of plasmonic layer structures with the strongest surface electromagnetic wave intensity.

(iii) Extract efficiency of plasmon induced hot electrons. Plasmon-induced hot electron injection is an important way to enhance the performance of photodetectors by LSPR. However, how to increase the extract efficiency of plasmon induced hot electrons in the plasmonic materials is still confused. To advance this field, a thorough understanding of plasmon energy distribution and transfer process of hot electrons is important. Deeper realization of these photon-electron behaviors will also inspire development of the related to high performance applications based on the plasmonic materials.

Declarations The authors declare that they have no competing interests and there are no conflicts.

Acknowledgements This work was financially supported by the National Natural Science Foundation of China (Nos. 22005267 and 22105011), the Basic Public Research Program of Zhejiang Province (Nos. LGF22B010004 and LY23B010001), the National Key Technologies R&D Program of China (No. 2022YFA1207000), the Research Funds of Hangzhou Institute for Advanced Study, UCAS (No. A05006C019001), and Hangzhou Science and Technology Bureau of Zhejiang Province (No. TD2020002).

References

1. A. Poglitsch, C. Waelkens, N. Geis, H. Feuchtgruber, B. Vandenbussche, et al., The photodetector array camera and spectrometer (PACS) on the Herschel space observatory, *Astron. Astrophys.* 518, L2 (2010)
2. R. A. Yotter and D. M. Wilson, A review of photodetectors for sensing light-emitting reporters in biological systems, *IEEE Sens. J.* 3(3), 288 (2003)
3. A. Casas, Clinical uses of 5-aminolaevulinic acid in photodynamic treatment and photodetection of cancer: A review, *Cancer Lett.* 490, 165 (2020)
4. W. Chen, T. Kan, Y. Ajiki, K. Matsumoto, and I. Shimoyama, NIR spectrometer using a Schottky photodetector enhanced by grating-based SPR, *Opt. Express* 24(22), 25797 (2016)
5. F. Rutz, A. Bächle, R. Aidam, J. Niemasz, W. Bronner, A. Zibold, and R. Rehm, InGaAs SWIR photodetectors for night vision, *Infrared Technology and Applications XLV* 11002, 202 (2019)
6. F. Rutz, R. Aidam, A. Bächle, H. Heussen, W. Bronner, R. Rehm, M. Benecke, S. Brunner, B. Göhler, P. Lutzmann, and A. Sieck, InGaAs-based SWIR photodetectors for night vision and gated viewing, *Electro-Optical and Infrared Systems: Technology and Applications XV* 10795, 1079503 (2018)
7. A. Pospischil, M. Humer, M. M. Furchi, D. Bachmann, R. Guider, T. Fromherz, and T. Mueller, CMOS-compatible graphene photodetector covering all optical communication bands, *Nat. Photonics* 7(11), 892 (2013)
8. C. Bao, J. Yang, S. Bai, W. Xu, Z. Yan, Q. Xu, J. Liu, W. Zhang, and F. Gao, High performance and stable all-inorganic metal halide perovskite-based photodetectors for optical communication applications, *Adv. Mater.* 30(38), 1803422 (2018)
9. A. Rogalski, Infrared detectors: Status and trends, *Prog. Quantum Electron.* 27(2–3), 59 (2003)
10. R. Liu, F. Wang, L. Liu, X. He, J. Chen, Y. Li, and T. Zhai, Band alignment engineering in two-dimensional transition metal dichalcogenide-based heterostructures for photodetectors, *Small Struct.* 2(3), 2000136 (2021)
11. S. Li, Y. Zhang, W. Yang, H. Liu, and X. Fang, 2D perovskite $Sr_2Nb_3O_{10}$ for high-performance UV photodetectors, *Adv. Mater.* 32(7), 1905443 (2020)
12. F. Koppens, T. Mueller, P. Avouris, A. Ferrari, M. S. Vitiello, and M. Polini, Photodetectors based on graphene, other two-dimensional materials and hybrid systems, *Nat. Nanotechnol.* 9(10), 780 (2014)
13. C. Xie, C. Mak, X. Tao, and F. Yan, Photodetectors based on two-dimensional layered materials beyond graphene, *Adv. Funct. Mater.* 27(19), 1603886 (2017)
14. X. Wang, P. Wang, J. Wang, W. Hu, X. Zhou, N. Guo, H. Huang, S. Sun, H. Shen, and T. Lin, Ultrasensitive and broadband MoS_2 photodetector driven by ferroelectrics, arXiv: 1502.04439 (2015)
15. T. Zhai, L. Li, X. Wang, X. Fang, Y. Bando, and D. Golberg, Recent developments in one-dimensional inorganic nanostructures for photodetectors, *Adv. Funct. Mater.* 20(24), 4233 (2010)
16. T. Zhai, X. Fang, M. Liao, X. Xu, H. Zeng, B. Yoshio, and D. Golberg, A comprehensive review of one-dimensional metal-oxide nanostructure photodetectors, *Sensors (Basel)* 9(8), 6504 (2009)
17. T. Zhai, L. Li, Y. Ma, M. Liao, X. Wang, X. Fang, J. Yao, Y. Bando, and D. Golberg, One-dimensional inorganic nanostructures: Synthesis, field-emission and photodetection, *Chem. Soc. Rev.* 40(5), 2986 (2011)
18. I. M. Asuo, D. Gedamu, I. Ka, L. F. Gerlein, F. X. Fortier, A. Pignolet, S. G. Cloutier, and R. Nechache, High-performance pseudo-halide perovskite nanowire networks for stable and fast-response photodetector, *Nano Energy* 51, 324 (2018)
19. S. X. Li, Y. S. Xu, C. L. Li, Q. Guo, G. Wang, H. Xia, H. H. Fang, L. Shen, and H. B. Sun, Perovskite single-crystal microwire-array photodetectors with performance stability beyond 1 year, *Adv. Mater.* 32(28), 2001998 (2020)
20. J. Wang, M. S. Gudiksen, X. Duan, Y. Cui, and C. M. Lieber, Highly polarized photoluminescence and photodetection from single indium phosphide nanowires, *Science* 293(5534), 1455 (2001)
21. S. Thunich, L. Prechtel, D. Spirkoska, G. Abstreiter, A. Fontcuberta i Morral, and A. W. Holleitner, Photocurrent and photoconductance properties of a GaAs nanowire, *Appl. Phys. Lett.* 95(8), 083111 (2009)
22. G. Konstantatos, I. Howard, A. Fischer, S. Hoogland, J. Clifford, E. Klem, L. Levina, and E. H. Sargent, Ultrasensitive solution-cast quantum dot photodetectors, *Nature* 442(7099), 180 (2006)
23. C. Livache, B. Martinez, N. Goubet, C. Gréboval, J. Qu, A. Chu, S. Royer, S. Ithurria, M. G. Silly, B. Dubertret, and E. Lhuillier, A colloidal quantum dot infrared photodetector and its use for intraband detection, *Nat. Commun.* 10(1), 2125 (2019)
24. Z. Ren, J. Sun, H. Li, P. Mao, Y. Wei, X. Zhong, J. Hu, S. Yang, and J. Wang, Bilayer PbS quantum dots for high-performance photodetectors, *Adv. Mater.* 29(33), 1702055 (2017)
25. J. Kim, S. M. Kwon, Y. K. Kang, Y. H. Kim, M. J. Lee, K. Han, A. Facchetti, M. G. Kim, and S. K. Park, A skin-like two-dimensionally pixelized full-color quantum dot photodetector, *Sci. Adv.* 5(11), eaax8801 (2019)
26. D. K. Gramotnev and S. I. Bozhevolnyi, Plasmonics beyond the diffraction limit, *Nat. Photonics* 4(2), 83 (2010)
27. J. Zhang, Y. Wang, D. Li, Y. Sun, and L. Jiang, Engineering surface plasmons in metal/nonmetal structures for highly desirable plasmonic photodetectors, *ACS Mater. Lett.* 4(2), 343 (2022)

28. H. Wang, S. Li, R. Ai, H. Huang, L. Shao, and J. Wang, Plasmonically enabled two-dimensional material-based optoelectronic devices, *Nanoscale* 12(15), 8095 (2020)
29. Y. Wang, J. Zhang, W. Liang, H. Yang, T. Guan, B. Zhao, Y. Sun, L. Chi, and L. Jiang, Rational design of plasmonic metal nanostructures for solar energy conversion, *CCS Chem.* 4(4), 1153 (2022)
30. J. Li, Z. Lou, and B. Li, Engineering plasmonic semiconductors for enhanced photocatalysis, *J. Mater. Chem. A* 9(35), 18818 (2021)
31. S. Li, P. Miao, Y. Zhang, J. Wu, B. Zhang, Y. Du, X. Han, J. Sun, and P. Xu, Recent advances in plasmonic nanostructures for enhanced photocatalysis and electrocatalysis, *Adv. Mater.* 33(6), 2000086 (2021)
32. W. Hou and S. B. Cronin, A review of surface plasmon resonance-enhanced photocatalysis, *Adv. Funct. Mater.* 23(13), 1612 (2013)
33. K. A. Willets and R. P. Van Duyne, Localized surface plasmon resonance spectroscopy and sensing, *Annu. Rev. Phys. Chem.* 58(1), 267 (2007)
34. L. J. Sherry, S. H. Chang, G. C. Schatz, R. P. Van Duyne, B. J. Wiley, and Y. Xia, Localized surface plasmon resonance spectroscopy of single silver nanocubes, *Nano Lett.* 5(10), 2034 (2005)
35. W. M. E. M. M. Daniyal, Y. W. Fen, J. Abdullah, A. R. Sadrolhosseini, and M. A. Mahdi, Design and optimization of surface plasmon resonance spectroscopy for optical constant characterization and potential sensing application: Theoretical and experimental approaches, *MDPI Photonics 8* (9), 361 (2021)
36. K. M. Mayer, F. Hao, S. Lee, P. Nordlander, and J. H. Hafner, A single molecule immunoassay by localized surface plasmon resonance, *Nanotechnology* 21(25), 255503 (2010)
37. P. Zijlstra, P. M. Paulo, and M. Orrit, Optical detection of single non-absorbing molecules using the surface plasmon resonance of a gold nanorod, *Nat. Nanotechnol.* 7(6), 379 (2012)
38. X. L. Zhou, Y. Yang, S. Wang, and X. W. Liu, Surface plasmon resonance microscopy: From single-molecule sensing to single-cell imaging, *Angew. Chem. Int. Ed.* 59(5), 1776 (2020)
39. L. Lan, Y. Gao, X. Fan, M. Li, Q. Hao, and T. Qiu, The origin of ultrasensitive SERS sensing beyond plasmonics, *Front. Phys.* 16(4), 43300 (2021)
40. H. Xu, Surface-enhanced Raman scattering beyond plasmonics, *Front. Phys.* 17(2), 23601 (2022)
41. Y. Zhang, F. Zhang, B. Du, H. Chen, S. Wageh, O. A. Al-Hartomy, A. G. Al-Sehemi, B. Zhang, and H. Zhang, Au/MXene based ultrafast all-optical switching, *Front. Phys.* 18(3), 33301 (2023)
42. S. Butun, N. A. Cinel, and E. Ozbay, LSPR enhanced MSM UV photodetectors, *Nanotechnology* 23(44), 444010 (2012)
43. N. Patra, M. Manikandan, V. Singh, and I. Palani, Investigations on LSPR effect of Cu/Al nanostructures on ZnO nanorods towards photodetector applications, *J. Lumin.* 238, 118331 (2021)
44. N. Gogurla, A. K. Sinha, S. Santra, S. Manna, and S. K. Ray, Multifunctional Au-ZnO plasmonic nanostructures for enhanced UV photodetector and room temperature NO sensing devices, *Sci. Rep.* 4(1), 6483 (2014)
45. A. S. Camacho, Plasmon nanolasers and plasmon optical tweezers, *J. Nano Sci. Tech.* 3, 10 (2015)
46. S. A. Maier, Plasmonics: Fundamentals and Applications, Springer, 2007, Vol. 1
47. G. Wiederrecht, Handbook of Nanoscale Optics and Electronics, Elsevier, 2010
48. J. A. Huang and L. B. Luo, Low-dimensional plasmonic photodetectors: Recent progress and future opportunities, *Adv. Opt. Mater.* 6(8), 1701282 (2018)
49. S. V. Boriskina, T. A. Cooper, L. Zeng, G. Ni, J. K. Tong, Y. Tsurimaki, Y. Huang, L. Meroueh, G. Mahan, and G. Chen, Losses in plasmonics: From mitigating energy dissipation to embracing loss-enabled functionalities, *Adv. Opt. Photonics* 9(4), 775 (2017)
50. P. B. Johnson and R. W. Christy, Optical constants of the noble metals, *Phys. Rev. B* 6(12), 4370 (1972)
51. C. Daboo, M. Baird, H. Hughes, N. Apsley, G. Jones, J. Frost, D. Peacock, and D. Ritchie, Surface-plasmon-enhanced photodetection in planar Au GaAs Schottky junctions, *Thin Solid Films* 189(1), 27 (1990)
52. T. Echtermeyer, S. Milana, U. Sassi, A. Eiden, M. Wu, E. Lidorikis, and A. Ferrari, Surface plasmon polariton graphene photodetectors, *Nano Lett.* 16(1), 8 (2016)
53. H. S. Ee, Y. S. No, J. Kim, H. G. Park, and M. K. Seo, Long-range surface plasmon polariton detection with a graphene photodetector, *Opt. Lett.* 43(12), 2889 (2018)
54. H. Zhang, M. Ijaz, and R. J. Blaikie, Recent review of surface plasmons and plasmonic hot electron effects in metallic nanostructures, *Front. Phys.* 18(6), 63602 (2023)
55. J. D. Jackson, Classical Electrodynamics, Wiley, 1999
56. W. H. Yang, G. C. Schatz, and R. P. Van Duyne, Discrete dipole approximation for calculating extinction and Raman intensities for small particles with arbitrary shapes, *J. Chem. Phys.* 103(3), 869 (1995)
57. K. Yee, Numerical solution of initial boundary value problems involving Maxwell's equations in isotropic media, *IEEE Trans. Antenn. Propag.* 14(3), 302 (1966)
58. J. M. Jin, The Finite Element Method in Electromagnetics, John Wiley & Sons, 2015
59. Jr Evanoff and G. Chumanov, Synthesis and optical properties of silver nanoparticles and arrays, *ChemPhysChem* 6(7), 1221 (2005)
60. M. Rycenga, C. M. Cobley, J. Zeng, W. Li, C. H. Moran, Q. Zhang, D. Qin, and Y. Xia, Controlling the synthesis and assembly of silver nanostructures for plasmonic applications, *Chem. Rev.* 111(6), 3669 (2011)
61. V. Amendola, R. Pilot, M. Frasconi, O. M. Maragò, and M. A. Iatì, Surface plasmon resonance in gold nanoparticles: A review, *J. Phys.: Condens. Matter* 29(20), 203002 (2017)
62. B. J. Wiley, S. H. Im, Z. Y. Li, J. McLellan, A. Siekkinen, and Y. Xia, Maneuvering the surface plasmon resonance of silver nanostructures through shape-controlled synthesis, *J. Phys. Chem. B* 110(32), 15666 (2006)

63. S. Link, M. B. Mohamed, and M. El-Sayed, Simulation of the optical absorption spectra of gold nanorods as a function of their aspect ratio and the effect of the medium dielectric constant, *J. Phys. Chem. B* 103(16), 3073 (1999)
64. J. Zeng, S. Roberts, and Y. Xia, Nanocrystal-based time-temperature indicators, *Chemistry* 16(42), 12559 (2010)
65. Y. Sun, B. Wiley, Z. Y. Li, and Y. Xia, Synthesis and optical properties of nanorattles and multiple-walled nanoshells/nanotubes made of metal alloys, *J. Am. Chem. Soc.* 126(30), 9399 (2004)
66. W. He, X. Wu, J. Liu, K. Zhang, W. Chu, L. Feng, X. Hu, W. Zhou, and S. Xie, Formation of AgPt alloy nanoislands via chemical etching with tunable optical and catalytic properties, *Langmuir* 26(6), 4443 (2010)
67. J. Chen, B. Wiley, J. McLellan, Y. Xiong, Z. Y. Li, and Y. Xia, Optical properties of Pd-Ag and Pt-Ag nanoboxes synthesized via galvanic replacement reactions, *Nano Lett.* 5(10), 2058 (2005)
68. S. Prathap Chandran, J. Ghatak, P. V. Satyam, and M. Sastry, Interfacial deposition of Ag on Au seeds leading to Aucore Ag shell in organic media, *J. Colloid Interface Sci.* 312(2), 498 (2007)
69. M. Liu and P. Guyot-Sionnest, Synthesis and optical characterization of Au/Ag core/shell nanorods, *J. Phys. Chem. B* 108(19), 5882 (2004)
70. M. D. Arnold and M. G. Blaber, Optical performance and metallic absorption in nanoplasmonic systems, *Opt. Express* 17(5), 3835 (2009)
71. M. Blaber, M. Arnold, N. Harris, M. Ford, and M. Cortie, Plasmon absorption in nanospheres: A comparison of sodium, potassium, aluminium, silver and gold, *Physica B* 394(2), 184 (2007)
72. G. H. Chan, J. Zhao, G. C. Schatz, and R. P. Van Duyne, Localized surface plasmon resonance spectroscopy of triangular aluminum nanoparticles, *J. Phys. Chem. C* 112(36), 13958 (2008)
73. S. K. Jha, Z. Ahmed, M. Agio, Y. Ekinci, and J. F. Löffler, Deep-UV surface-enhanced resonance Raman scattering of adenine on aluminum nanoparticle arrays, *J. Am. Chem. Soc.* 134(4), 1966 (2012)
74. I. Zorić, M. Zach, B. Kasemo, and C. Langhammer, Gold, platinum, and aluminum nanodisk plasmons: Material independence, subradiance, and damping mechanisms, *ACS Nano* 5(4), 2535 (2011)
75. M. Castro-Lopez, D. Brinks, R. Sapienza, and N. F. Van Hulst, Aluminum for nonlinear plasmonics: Resonance-driven polarized luminescence of Al, Ag, and Au nanoantennas, *Nano Lett.* 11(11), 4674 (2011)
76. T. Stöckli, J. M. Bonard, P. A. Stadelmann, and A. Châtelain, EELS investigation of plasmon excitations in aluminum nanospheres and carbon nanotubes, *Z. Phys. D At. Mol. Clust.* 40(1–4), 425 (1997)
77. A. Taguchi, Y. Saito, K. Watanabe, S. Yijian, and S. Kawata, Tailoring plasmon resonances in the deep-ultraviolet by size-tunable fabrication of aluminum nanostructures, *Appl. Phys. Lett.* 101(8), 081110 (2012)
78. M. W. Knight, L. Liu, Y. Wang, L. Brown, S. Mukherjee, N. S. King, H. O. Everitt, P. Nordlander, and N. J. Halas, Aluminum plasmonic nanoantennas, *Nano Lett.* 12(11), 6000 (2012)
79. A. Dubey, R. Mishra, Y. H. Hsieh, C. W. Cheng, B. H. Wu, L. J. Chen, S. Gwo, and T. J. Yen, Aluminum plasmonics enriched ultraviolet GaN photodetector with ultrahigh responsivity, detectivity, and broad bandwidth, *Adv. Sci. (Weinh.)* 7(24), 2002274 (2020)
80. M. Li, M. Shi, B. Wang, C. Zhang, S. Yang, Y. Yang, N. Zhou, X. Guo, D. Chen, S. Li, H. Mao, and J. Xiong, Quasi-ordered nanoforests with hybrid plasmon resonances for broadband absorption and photodetection, *Adv. Funct. Mater.* 31(38), 2102840 (2021)
81. J. Li, C. Nie, F. Sun, L. Tang, Z. Zhang, J. Zhang, Y. Zhao, J. Shen, S. Feng, H. Shi, and X. Wei, Enhancement of the photoresponse of monolayer MoS_2 photodetectors induced by a nanoparticle grating, *ACS Appl. Mater. Interfaces* 12(7), 8429 (2020)
82. Z. Chen, X. Li, J. Wang, L. Tao, M. Long, S. J. Liang, L. K. Ang, C. Shu, H. K. Tsang, and J. B. Xu, Synergistic effects of plasmonics and electron trapping in graphene short-wave infrared photodetectors with ultrahigh responsivity, *ACS Nano* 11(1), 430 (2017)
83. B. L. Greenberg, S. Ganguly, J. T. Held, N. J. Kramer, K. A. Mkhoyan, E. S. Aydil, and U. R. Kortshagen, Nonequilibrium-plasma-synthesized ZnO nanocrystals with plasmon resonance tunable via Al doping and quantum confinement, *Nano Lett.* 15(12), 8162 (2015)
84. A. M. Schimpf, C. E. Gunthardt, J. D. Rinehart, J. M. Mayer, and D. R. Gamelin, Controlling carrier densities in photochemically reduced colloidal ZnO nanocrystals: Size dependence and role of the hole quencher, *J. Am. Chem. Soc.* 135(44), 16569 (2013)
85. G. Garcia, R. Buonsanti, E. L. Runnerstrom, R. J. Mendelsberg, A. Llordes, A. Anders, T. J. Richardson, and D. J. Milliron, Dynamically modulating the surface plasmon resonance of doped semiconductor nanocrystals, *Nano Lett.* 11(10), 4415 (2011)
86. T. R. Gordon, T. Paik, D. R. Klein, G. V. Naik, H. Caglayan, A. Boltasseva, and C. B. Murray, Shape-dependent plasmonic response and directed self-assembly in a new semiconductor building block, indium-doped cadmium oxide (ICO), *Nano Lett.* 13(6), 2857 (2013)
87. Q. Liu, C. Sun, Q. He, D. Liu, A. Khalil, T. Xiang, Z. Wu, J. Wang, and L. Song, Ultrathin carbon layer coated MoO_2 nanoparticles for high-performance near-infrared photothermal cancer therapy, *Chem. Commun. (Camb.)* 51(49), 10054 (2015)
88. T. M. Mattox, A. Bergerud, A. Agrawal, and D. J. Milliron, Influence of shape on the surface plasmon resonance of tungsten bronze nanocrystals, *Chem. Mater.* 26(5), 1779 (2014)
89. J. M. Luther, P. K. Jain, T. Ewers, and A. P. Alivisatos, Localized surface plasmon resonances arising from free carriers in doped quantum dots, *Nat. Mater.* 10(5), 361 (2011)
90. V. Gurin, V. Prokopenko, A. Alexeenko, S. Wang, K. Yumashev, and P. Prokoshin, Sol–gel silica glasses with nanoparticles of copper selenide: Synthesis, optics and structure, *Int. J. Inorg. Mater.* 3(6), 493 (2001)
91. B. C. Marin, S. W. Hsu, L. Chen, A. Lo, D. W. Zwissler, Z. Liu, and A. R. Tao, Plasmon-enhanced

two-photon absorption in photoluminescent semiconductor nanocrystals, *ACS Photonics* 3(4), 526 (2016)
92. D. J. Rowe, J. S. Jeong, K. A. Mkhoyan, and U. R. Kortshagen, Phosphorus-doped silicon nanocrystals exhibiting mid-infrared localized surface plasmon resonance, *Nano Lett.* 13(3), 1317 (2013)
93. R. Buonsanti, A. Llordes, S. Aloni, B. A. Helms, and D. J. Milliron, Tunable infrared absorption and visible transparency of colloidal aluminum-doped zinc oxide nanocrystals, *Nano Lett.* 11(11), 4706 (2011)
94. S. Ghosh, M. Saha, and S. K. De, Tunable surface plasmon resonance and enhanced electrical conductivity of In doped ZnO colloidal nanocrystals, *Nanoscale* 6(12), 7039 (2014)
95. M. Kanehara, H. Koike, T. Yoshinaga, and T. Teranishi, Indium tin oxide nanoparticles with compositionally tunable surface plasmon resonance frequencies in the near-IR region, *J. Am. Chem. Soc.* 131(49), 17736 (2009)
96. C. Y. Su and H. C. Lin, Direct route to tungsten oxide nanorod bundles: Microstructures and electro-optical properties, *J. Phys. Chem. C* 113(10), 4042 (2009)
97. S. H. Lee, H. Nishi, and T. Tatsuma, Tunable plasmon resonance of molybdenum oxide nanoparticles synthesized in non-aqueous media, *Chem. Commun. (Camb.)* 53(94), 12680 (2017)
98. A. M. Schimpf, S. D. Lounis, E. L. Runnerstrom, D. J. Milliron, and D. R. Gamelin, Redox chemistries and plasmon energies of photodoped In_2O_3 and Sn-doped In_2O_3 (ITO) nanocrystals, *J. Am. Chem. Soc.* 137(1), 518 (2015)
99. J. A. Faucheaux and P. K. Jain, Plasmons in photocharged ZnO nanocrystals revealing the nature of charge dynamics, *J. Phys. Chem. Lett.* 4(18), 3024 (2013)
100. H. Du, Y. Li, N. Zhou, C. Pu, J. Yin, X. Kong, H. Tian, and Y. Jin, Plasmonic metal oxide nanocrystals via surface anchoring of redox-active phosphorus species, *Chem. Mater.* 33(13), 5290 (2021)
101. C. N. Valdez, M. Braten, A. Soria, D. R. Gamelin, and J. M. Mayer, Effect of protons on the redox chemistry of colloidal zinc oxide nanocrystals, *J. Am. Chem. Soc.* 135(23), 8492 (2013)
102. R. Lu, C. W. Ge, Y. F. Zou, K. Zheng, D. D. Wang, T. F. Zhang, and L. B. Luo, A localized surface plasmon resonance and light confinement-enhanced near-infrared light photodetector, *Laser Photonics Rev.* 10(4), 595 (2016)
103. Z. Ni, L. Ma, S. Du, Y. Xu, M. Yuan, H. Fang, Z. Wang, M. Xu, D. Li, J. Yang, W. Hu, X. Pi, and D. Yang, Plasmonic silicon quantum dots enabled high-sensitivity ultrabroadband photodetection of graphene-based hybrid phototransistors, *ACS Nano* 11(10), 9854 (2017)
104. M. Abb, Y. Wang, N. Papasimakis, C. De Groot, and O. L. Muskens, Surface-enhanced infrared spectroscopy using metal oxide plasmonic antenna arrays, *Nano Lett.* 14(1), 346 (2014)
105. A. Agrawal, I. Kriegel, and D. J. Milliron, Shape-dependent field enhancement and plasmon resonance of oxide nanocrystals, *J. Phys. Chem. C* 119(11), 6227 (2015)
106. E. L. Runnerstrom, A. Bergerud, A. Agrawal, R. W. Johns, C. J. Dahlman, A. Singh, S. M. Selbach, and D. J. Milliron, Defect engineering in plasmonic metal oxide nanocrystals, *Nano Lett.* 16(5), 3390 (2016)
107. J. Kim, A. Agrawal, F. Krieg, A. Bergerud, and D. J. Milliron, The interplay of shape and crystalline anisotropies in plasmonic semiconductor nanocrystals, *Nano Lett.* 16(6), 3879 (2016)
108. B. Auguié and W. L. Barnes, Collective resonances in gold nanoparticle arrays, *Phys. Rev. Lett.* 101(14), 143902 (2008)
109. Y. A. Urzhumov, G. Shvets, J. Fan, F. Capasso, D. Brandl, and P. Nordlander, Plasmonic nanoclusters: A path towards negative-index metafluids, *Opt. Express* 15(21), 14129 (2007)
110. E. Boulais, R. Lachaine, A. Hatef, and M. Meunier, Plasmonics for pulsed-laser cell nanosurgery: Fundamentals and applications, *J. Photochem. Photobiol. Photochem. Rev.* 17, 26 (2013)
111. A. Yurtsever and A. H. Zewail, Direct visualization of near-fields in nanoplasmonics and nanophotonics, *Nano Lett.* 12(6), 3334 (2012)
112. Y. Dong, Y. Gu, Y. Zou, J. Song, L. Xu, J. Li, J. Xue, X. Li, and H. Zeng, Improving all-inorganic perovskite photodetectors by preferred orientation and plasmonic effect, *Small* 12(40), 5622 (2016)
113. H. A. Atwater and A. Polman, Plasmonics for improved photovoltaic devices, *Nat. Mater.* 9(3), 205 (2010)
114. A. Furube, T. Yoshinaga, M. Kanehara, M. Eguchi, and T. Teranishi, Electric-field enhancement inducing near-infrared two-photon absorption in an indium-tin oxide nanoparticle film, *Angew. Chem. Int. Ed.* 51(11), 2640 (2012)
115. A. Agrawal, A. Singh, S. Yazdi, A. Singh, G. K. Ong, K. Bustillo, R. W. Johns, E. Ringe, and D. J. Milliron, Resonant coupling between molecular vibrations and localized surface plasmon resonance of faceted metal oxide nanocrystals, *Nano Lett.* 17(4), 2611 (2017)
116. C. Sönnichsen, T. Franzl, T. Wilk, G. von Plessen, J. Feldmann, O. Wilson, and P. Mulvaney, Drastic reduction of plasmon damping in gold nanorods, *Phys. Rev. Lett.* 88(7), 077402 (2002)
117. M. L. Brongersma, N. J. Halas, and P. Nordlander, Plasmon-induced hot carrier science and technology, *Nat. Nanotechnol.* 10(1), 25 (2015)
118. M. W. Knight, Y. Wang, A. S. Urban, A. Sobhani, B. Y. Zheng, P. Nordlander, and N. J. Halas, Embedding plasmonic nanostructure diodes enhances hot electron emission, *Nano Lett.* 13(4), 1687 (2013)
119. J. Lehmann, M. Merschdorf, W. Pfeiffer, A. Thon, S. Voll, and G. Gerber, Surface plasmon dynamics in silver nanoparticles studied by femtosecond time-resolved photoemission, *Phys. Rev. Lett.* 85(14), 2921 (2000)
120. M. W. Knight, H. Sobhani, P. Nordlander, and N. J. Halas, Photodetection with active optical antennas, *Science* 332(6030), 702 (2011)
121. H. Chalabi, D. Schoen, and M. L. Brongersma, Hot-electron photodetection with a plasmonic nanostripe

antenna, *Nano Lett.* 14(3), 1374 (2014)
122. G. Zhao, H. Kozuka, and T. Yoko, Sol–gel preparation and photoelectrochemical properties of TiO_2 films containing Au and Ag metal particles, *Thin Solid Films* 277(1-2), 147 (1996)
123. Y. Tian and T. Tatsuma, Plasmon-induced photoelectrochemistry at metal nanoparticles supported on nanoporous TiO_2, *Chem. Commun. (Camb.)* (16), 1810 (2004)
124. Y. Tian and T. Tatsuma, Mechanisms and applications of plasmon-induced charge separation at TiO_2 films loaded with gold nanoparticles, *J. Am. Chem. Soc.* 127(20), 7632 (2005)
125. S. Linic, P. Christopher, and D. B. Ingram, Plasmonic-metal nanostructures for efficient conversion of solar to chemical energy, *Nat. Mater.* 10(12), 911 (2011)
126. S. Mubeen, J. Lee, N. Singh, S. Krämer, G. D. Stucky, and M. Moskovits, An autonomous photosynthetic device in which all charge carriers derive from surface plasmons, *Nat. Nanotechnol.* 8(4), 247 (2013)
127. D. Peters, An infrared detector utilizing internal photoemission, *Proc. IEEE* 55(5), 704 (1967)
128. A. Akbari and P. Berini, Schottky contact surface-plasmon detector integrated with an asymmetric metal stripe waveguide, *Appl. Phys. Lett.* 95(2), 021104 (2009)
129. I. Goykhman, B. Desiatov, J. Khurgin, J. Shappir, and U. Levy, Locally oxidized silicon surface-plasmon Schottky detector for telecom regime, *Nano Lett.* 11(6), 2219 (2011)
130. C. Scales and P. Berini, Thin-film Schottky barrier photodetector models, *IEEE J. Quantum Electron.* 46(5), 633 (2010)
131. S. Faris, T. Gustafson, and J. Wiesner, Detection of optical and infrared radiation with DC-biased electron-tunneling metal–barrier–metal diodes, *IEEE J. Quantum Electron.* 9(7), 737 (1973)
132. M. Heiblum, S. Wang, J. Whinnery, and T. Gustafson, Characteristics of integrated MOM junctions at dc and at optical frequencies, *IEEE J. Quantum Electron.* 14(3), 159 (1978)
133. X. Li, D. Xiao, and Z. Zhang, Landau damping of quantum plasmons in metal nanostructures, *New J. Phys.* 15(2), 023011 (2013)
134. K. Watanabe, D. Menzel, N. Nilius, and H. J. Freund, Photochemistry on metal nanoparticles, *Chem. Rev.* 106(10), 4301 (2006)
135. J. B. Khurgin, How to deal with the loss in plasmonics and metamaterials, *Nat. Nanotechnol.* 10(1), 2 (2015)
136. Y. Ben-Shahar, F. Scotognella, N. Waiskopf, I. Kriegel, S. Dal Conte, G. Cerullo, and U. Banin, Effect of surface coating on the photocatalytic function of hybrid CdS–Au nanorods, *Small* 11(4), 462 (2015)
137. Y. Ben-Shahar, F. Scotognella, I. Kriegel, L. Moretti, G. Cerullo, E. Rabani, and U. Banin, Optimal metal domain size for photocatalysis with hybrid semiconductor –metal nanorods, *Nat. Commun.* 7(1), 10413 (2016)
138. L. Du, A. Furube, K. Hara, R. Katoh, and M. Tachiya, Ultrafast plasmon induced electron injection mechanism in gold–TiO_2 nanoparticle system, *J. Photochem. Photobiol. Photochem. Rev.* 15, 21 (2013)
139. A. Furube, L. Du, K. Hara, R. Katoh, and M. Tachiya, Ultrafast plasmon-induced electron transfer from gold nanodots into TiO_2 nanoparticles, *J. Am. Chem. Soc.* 129(48), 14852 (2007)
140. L. Du, A. Furube, K. Yamamoto, K. Hara, R. Katoh, and M. Tachiya, Plasmon-induced charge separation and recombination dynamics in gold–TiO_2 nanoparticle systems: dependence on TiO_2 particle size, *J. Phys. Chem. C* 113(16), 6454 (2009)
141. T. Liu, Q. Wang, C. Zhang, X. Li, and J. Hu, High performance of hot-carrier generation, transport and injection in TiN/TiO_2 junction, *Front. Phys.* 17(5), 53509 (2022)
142. W. Yang, Y. Liu, D. A. Cullen, J. R. McBride, and T. Lian, Harvesting sub-bandgap IR photons by photothermionic hot electron transfer in a plasmonic p–n junction, *Nano Lett.* 21(9), 4036 (2021)
143. A. O. Govorov, H. Zhang, and Y. K. Gun'ko, Theory of photoinjection of hot plasmonic carriers from metal nanostructures into semiconductors and surface molecules, *J. Phys. Chem. C* 117(32), 16616 (2013)
144. A. Manjavacas, J. G. Liu, V. Kulkarni, and P. Nordlander, Plasmon-induced hot carriers in metallic nanoparticles, *ACS Nano* 8(8), 7630 (2014)
145. R. Sundararaman, P. Narang, A. S. Jermyn, III Goddard, and H. A. Atwater, Theoretical predictions for hot-carrier generation from surface plasmon decay, *Nat. Commun.* 5(1), 5788 (2014)
146. L. Ranno, S. D. Forno, and J. Lischner, Computational design of bimetallic core–shell nanoparticles for hot-carrier photocatalysis, *npj Comput, Mater.* 4(1), 31 (2018)
147. M. Bernardi, D. Vigil-Fowler, C. S. Ong, J. B. Neaton, and S. G. Louie, *Ab initio* study of hot electrons in GaAs, *Proc. Natl. Acad. Sci. USA* 112(17), 5291 (2015)
148. Z. Lian, M. Sakamoto, H. Matsunaga, J. J. M. Vequizo, A. Yamakata, M. Haruta, H. Kurata, W. Ota, T. Sato, and T. Teranishi, Near infrared light induced plasmonic hot hole transfer at a nano-heterointerface, *Nat. Commun.* 9(1), 2314 (2018)
149. F. Hao, Y. Sonnefraud, P. V. Dorpe, S. A. Maier, N. J. Halas, and P. Nordlander, Symmetry breaking in plasmonic nanocavities: Subradiant LSPR sensing and a tunable Fano resonance, *Nano Lett.* 8(11), 3983 (2008)
150. Y. Zhang, Theory of plasmonic hot-carrier generation and relaxation, *J. Phys. Chem. A* 125(41), 9201 (2021)
151. M. A. Butt, Metal–insulator–metal waveguide-based plasmonic sensors: Fantasy or truth — A critical review, *Appl. Res.* 2, e202200099 (2023)
152. W. Y. Kong, G. A. Wu, K. Y. Wang, T. F. Zhang, Y. F. Zou, D. D. Wang, and L. B. Luo, Graphene-β-Ga_2O_3 heterojunction for highly sensitive deep UV photodetector application, *Adv. Mater.* 28(48), 10725 (2016)
153. X. Wang, K. Liu, X. Chen, B. Li, M. Jiang, Z. Zhang, H. Zhao, and D. Shen, Highly wavelength-selective enhancement of responsivity in Ag nanoparticle-modified ZnO UV photodetector, *ACS Appl. Mater. Interfaces* 9(6), 5574 (2017)
154. W. Ouyang, F. Teng, M. Jiang, and X. Fang, ZnO

film UV photodetector with enhanced performance: Heterojunction with $CdMoO_4$ microplates and the hot electron injection effect of Au nanoparticles, *Small* 13(39), 1702177 (2017)

155. S. Liu, M. Y. Li, D. Su, M. Yu, H. Kan, H. Liu, X. Wang, and S. Jiang, Broad-band high-sensitivity ZnO colloidal quantum dots/self-assembled Au nanoantennas heterostructures photodetectors, *ACS Appl. Mater. Interfaces* 10(38), 32516 (2018)
156. M. Li, M. Zhao, D. Jiang, M. Yang, Q. Li, C. Shan, X. Zhou, Y. Duan, N. Wang, and J. Sun, Optimizing the spacing of Ag nanoparticle layers to enhance the performance of ZnO/Ag/ZnO/Ag/ZnO multilayer-structured UV photodetectors, *Sens. Actuators A Phys.* 297, 111501 (2019)
157. Y. Liu, X. Zhang, J. Su, H. Li, Q. Zhang, and Y. Gao, Ag nanoparticles@ ZnO nanowire composite arrays: An absorption enhanced UV photodetector, *Opt. Express* 22(24), 30148 (2014)
158. J. Lu, C. Xu, J. Dai, J. Li, Y. Wang, Y. Lin, and P. Li, Improved UV photoresponse of ZnO nanorod arrays by resonant coupling with surface plasmons of Al nanoparticles, *Nanoscale* 7(8), 3396 (2015)
159. C. C. Yang, H. C. Yu, Y. K. Su, M. Y. Chuang, C. H. Hsiao, and T. H. Kao, Noise properties of ag nanoparticle-decorated ZnO nanorod UV photodetectors, *IEEE Photonics Technol. Lett.* 28(4), 379 (2016)
160. C. L. Hsu, Y. C. Wang, S. P. Chang, and S. J. Chang, Ultraviolet/visible photodetectors based on p–n NiO/ZnO nanowires decorated with Pd nanoparticles, *ACS Appl. Nano Mater.* 2(10), 6343 (2019)
161. Y. Noh, J. Shin, H. Lee, G. Y. Kim, M. Kumar, and D. Lee, Decoration of Ag nanoparticle on ZnO nanowire by intense pulsed light and enhanced UV photodetector, *Chemosensors (Basel)* 9(11), 321 (2021)
162. M. Y. Li, S. Liu, Z. Huang, Y. Ai, K. Shen, H. Lu, M. Li, and J. Wu, Facile fabrication of ultrasensitive honeycomb nano-mesh ultraviolet photodetectors based on self-assembled plasmonic architectures, *ACS Appl. Mater. Interfaces* 13(30), 35972 (2021)
163. Q. Li, J. Huang, J. Meng, and Z. Li, Enhanced performance of a self-powered ZnO photodetector by coupling LSPR-inspired pyro-phototronic effect and piezo-phototronic effect, *Adv. Opt. Mater.* 10(7), 2102468 (2022)
164. L. Goswami, N. Aggarwal, S. Krishna, M. Singh, P. Vashishtha, S. P. Singh, S. Husale, R. Pandey, and G. Gupta, Au-nanoplasmonics-mediated surface plasmon-enhanced GaN nanostructured UV photodetectors, *ACS Omega* 5(24), 14535 (2020)
165. S. Kunwar, S. Pandit, J. H. Jeong, and J. Lee, Improved photoresponse of UV photodetectors by the incorporation of plasmonic nanoparticles on GaN through the resonant coupling of localized surface plasmon resonance, *Nano-Micro Lett.* 12(1), 91 (2020)
166. S. Lin, R. Kulkarni, R. Mandavkar, M. A. Habib, S. Burse, S. Kunwar, and J. Lee, Surmounting the interband threshold limit by the hot electron excitation of multimetallic plasmonic AgAuCu NPs for UV photodetector application, *CrystEngComm* 24(22), 4134 (2022)
167. K. Arora, D. P. Singh, P. Fischer, and M. Kumar, Spectrally selective and highly sensitive UV photodetection with UV-A, C band specific polarity switching in silver plasmonic nanoparticle enhanced gallium oxide thin-film, *Adv. Opt. Mater.* 8(16), 2000212 (2020)
168. Y. Liu, W. Chen, L. Zhao, J. Guo, C. Yang, X. Wang, W. Huang, T. Ren, and J. Xu, Plasmon-enhanced InGaZnO ultraviolet photodetectors tuned by ferroelectric HfZrO, *Adv. Electron. Mater.* 5(12), 1900588 (2019)
169. S. Han, H. Xia, Y. Lu, S. Hu, D. Zhang, W. Xu, M. Fang, W. Liu, P. Cao, and D. Zhu, Great enhancement effect of 20–40 nm Ag NPs on solar-blind UV response of the mixed-phase MgZnO detector, *ACS Omega* 6(10), 6699 (2021)
170. X. Shi, Z. Yang, S. Yin, and H. Zeng, Al plasmon-enhanced diamond solar-blind UV photodetector by coupling of plasmon and excitons, *Mater. Technol.* 31(9), 544 (2016)
171. S. Mondal, A. Dalal, and A. Mondal, Al nanoparticles decorated Er: TiO_2 thin film based plasmonic photodetector, *Ceram. Int.* 49(4), 6289 (2023)
172. Z. Fang, Z. Liu, Y. Wang, P. M. Ajayan, P. Nordlander, and N. J. Halas, Graphene-antenna sandwich photodetector, *Nano Lett.* 12(7), 3808 (2012)
173. S. Lee, M. Lee, H. Shin, and D. Choi, Control of density and LSPR of Au nanoparticles on graphene, *Nanotechnology* 24(27), 275702 (2013)
174. S. Jang, E. Hwang, Y. Lee, S. Lee, and J. H. Cho, Multifunctional graphene optoelectronic devices capable of detecting and storing photonic signals, *Nano Lett.* 15(4), 2542 (2015)
175. J. Miao, W. Hu, Y. Jing, W. Luo, L. Liao, A. Pan, S. Wu, J. Cheng, X. Chen, and W. Lu, Surface plasmon-enhanced photodetection in few layer MoS_2 phototransistors with Au nanostructure arrays, *Small* 11(20), 2392 (2015)
176. V. Selamneni, H. Raghavan, A. Hazra, and P. Sahatiya, MoS_2/paper decorated with metal nanoparticles (Au, Pt, and Pd) based plasmonic-enhanced broadband (visible-NIR) flexible photodetectors, *Adv. Mater. Interfaces* 8(6), 2001988 (2021)
177. G. Li, Y. Song, S. Feng, L. Feng, Z. Liu, B. Leng, Z. Fu, J. Li, X. Jiang, B. Liu, and X. Zhang, Improved optoelectronic performance of MoS_2 photodetector via localized surface plasmon resonance coupling of double-layered Au nanoparticles with sandwich structure, *ACS Appl. Electron. Mater.* 4(4), 1626 (2022)
178. Y. Li, J. G. DiStefano, A. A. Murthy, J. D. Cain, E. D. Hanson, Q. Li, F. C. Castro, X. Chen, and V. P. Dravid, Superior plasmonic photodetectors based on Au@MoS_2 core–shell heterostructures, *ACS Nano* 11(10), 10321 (2017)
179. J. Zhang, X. Zhang, J. Li, Z. Ma, B. Leng, Q. Xia, L. Shen, Y. Song, Z. Fu, S. Feng, L. Feng, Z. Liu, S. Yuldashev, X. Jiang, and B. Liu, Simultaneous visible and ultraviolet photoresponse improvement of MoS_2/ZnO heterostructure photodetector via direct resonant coupling of Au nanoparticles localized surface plasmon resonance, *Opt. Mater.* 124, 111997 (2022)
180. A. J. Hoffman, L. Alekseyev, S. S. Howard, K. J.

Franz, D. Wasserman, V. A. Podolskiy, E. E. Narimanov, D. L. Sivco, and C. Gmachl, Negative refraction in semiconductor metamaterials, *Nat. Mater.* 6(12), 946 (2007)
181. Z. Fang, Y. Wang, A. E. Schlather, Z. Liu, P. M. Ajayan, F. J. García de Abajo, P. Nordlander, X. Zhu, and N. J. Halas, Active tunable absorption enhancement with graphene nanodisk arrays, *Nano Lett.* 14(1), 299 (2014)
182. Z. Xia, P. Li, Y. Wang, T. Song, Q. Zhang, and B. Sun, Solution-processed gold nanorods integrated with graphene for near-infrared photodetection via hot carrier injection, *ACS Appl. Mater. Interfaces* 7(43), 24136 (2015)
183. B. Deng, Q. Guo, C. Li, H. Wang, X. Ling, D. B. Farmer, S. Han, J. Kong, and F. Xia, Coupling-enhanced broadband mid-infrared light absorption in graphene plasmonic nanostructures, *ACS Nano* 10(12), 11172 (2016)
184. N. S. Rohizat, A. H. A. Ripain, C. S. Lim, C. L. Tan, and R. Zakaria, Plasmon-enhanced reduced graphene oxide photodetector with monometallic of Au and Ag nanoparticles at VIS–NIR region, *Sci. Rep.* 11(1), 19688 (2021)
185. Z. B. Dai, G. Cen, Z. Zhang, X. Lv, K. Liu, and Z. Li, Near-field infrared response of graphene on copper substrate, *Front. Phys.* 17(4), 43502 (2022)
186. S. Podder and A. R. Pal, Plasmonic visible-NIR photodetector based on hot electrons extracted from nanostructured titanium nitride, *J. Appl. Phys.* 126(8), 083108 (2019)
187. A. Lesuffleur, H. Im, N. C. Lindquist, and S. H. Oh, Periodic nanohole arrays with shape-enhanced plasmon resonance as real-time biosensors, *Appl. Phys. Lett.* 90(24), 243110 (2007)
188. P. C. Chuang, P. C. Liao, and Y. F. Chen, Enhancing the sensitivity of localized surface plasmon resonance (LSPR) biosensors using nanorods and DNA aptamers, *Plasmonics in Biology and Medicine XII* 2015, 98
189. H. Takei, N. Bessho, A. Ishii, T. Okamoto, A. Beyer, H. Vieker, and A. Gölzhäuser, Enhanced infrared LSPR sensitivity of cap-shaped gold nanoparticles coupled to a metallic film, *Langmuir* 30(8), 2297 (2014)
190. M. Bauch, K. Toma, M. Toma, Q. Zhang, and J. Dostalek, Plasmon-enhanced fluorescence biosensors: A review, *Plasmonics* 9(4), 781 (2014)
191. A. Campion and P. Kambhampati, Surface-enhanced Raman scattering, *Chem. Soc. Rev.* 27(4), 241 (1998)
192. L. Tang and J. Li, Plasmon-based colorimetric nanosensors for ultrasensitive molecular diagnostics, *ACS Sens.* 2(7), 857 (2017)
193. S. Chen, M. Svedendahl, R. P. Van Duyne, and M. Käll, Plasmon-enhanced colorimetric ELISA with single molecule sensitivity, *Nano Lett.* 11(4), 1826 (2011)
194. Y. Liang, H. Zhang, W. Zhu, A. Agrawal, H. Lezec, L. Li, W. Peng, Y. Zou, Y. Lu, and T. Xu, Subradiant dipolar interactions in plasmonic nanoring resonator array for integrated label-free biosensing, *ACS Sens.* 2(12), 1796 (2017)
195. X. Wang, J. Zhu, H. Tong, X. Yang, X. Wu, Z. Pang, H. Yang, and Y. Qi, A theoretical study of a plasmonic sensor comprising a gold nano-disk array on gold film with a SiO_2 spacer, *Chin. Phys. B* 28(4), 044201 (2019)
196. T. Chen, S. Li, and H. Sun, Metamaterials application in sensing, *Sensors (Basel)* 12(3), 2742 (2012)
197. C. Wu, A. B. Khanikaev, R. Adato, N. Arju, A. A. Yanik, H. Altug, and G. Shvets, Fano-resonant asymmetric metamaterials for ultrasensitive spectroscopy and identification of molecular monolayers, *Nat. Mater.* 11(1), 69 (2012)
198. J. Zhu, Z. Wang, S. Lin, S. Jiang, X. Liu, and S. Guo, Low-cost flexible plasmonic nanobump metasurfaces for label-free sensing of serum tumor marker, *Biosens. Bioelectron.* 150, 111905 (2020)
199. Y. I. Park, H. Im, R. Weissleder, and H. Lee, Nanostar clustering improves the sensitivity of plasmonic assays, *Bioconjug. Chem.* 26(8), 1470 (2015)
200. H. Cheng, T. Kamegawa, K. Mori, and H. Yamashita, Surfactant-free nonaqueous synthesis of plasmonic molybdenum oxide nanosheets with enhanced catalytic activity for hydrogen generation from ammonia borane under visible light, *Angew. Chem. Int. Ed.* 53(11), 2910 (2014)
201. Z. Zhang, J. Huang, Y. Fang, M. Zhang, K. Liu, and B. Dong, A nonmetal plasmonic Z-scheme photocatalyst with UV- to NIR-driven photocatalytic protons reduction, *Adv. Mater.* 29(18), 1606688 (2017)
202. Z. Lou, M. Zhu, X. Yang, Y. Zhang, M. H. Whangbo, B. Li, and B. Huang, Continual injection of photoinduced electrons stabilizing surface plasmon resonance of non-elemental-metal plasmonic photocatalyst CdS/WO_{3-x} for efficient hydrogen generation, *Appl. Catal. B* 226, 10 (2018)
203. L. Mikac, M. Ivanda, M. Gotić, T. Mihelj, and L. Horvat, Synthesis and characterization of silver colloidal nanoparticles with different coatings for SERS application, *J. Nanopart. Res.* 16(12), 2748 (2014)
204. H. Y. Chen, M. H. Lin, C. Y. Wang, Y. M. Chang, and S. Gwo, Large-scale hot spot engineering for quantitative SERS at the single-molecule scale, *J. Am. Chem. Soc.* 137(42), 13698 (2015)
205. Y. Zhou, R. Ding, P. Joshi, and P. Zhang, Quantitative surface-enhanced Raman measurements with embedded internal reference, *Anal. Chim. Acta* 874, 49 (2015)